

Pair Distribution Function Analysis of the Short-Range Magnetic and
Atomic Correlations in Manganese Telluride

Jacob Andrew Christensen

A senior thesis submitted to the faculty of
Brigham Young University
in partial fulfillment of the requirements for the degree of
Bachelor of Science

Benjamin Frandsen, Advisor

Department of Physics and Astronomy

Brigham Young University

April 2022

Copyright © 2022 Jacob Andrew Christensen

All Rights Reserved

ABSTRACT

Pair Distribution Function Analysis of the Short-Range Magnetic and Atomic Correlations in Manganese Telluride

Jacob Andrew Christensen
Department of Physics and Astronomy, BYU
Bachelor of Science

The antiferromagnetic semiconductor MnTe has recently been identified as a candidate high-performance thermoelectric, with its short-range magnetic correlations playing a crucial role in this technological application. Previous research has shown that these correlations are a significant contributor to the high thermoelectric figure of merit zT in MnTe through a mechanism known as paramagnon drag. However, a clear picture of the nature of these correlations has not been developed up until this point. Here, we present three-dimensional atomic and magnetic pair distribution function (PDF) analysis of neutron total scattering data collected from a single crystal of MnTe, along with PDF data obtained from pure and doped MnTe powders. These complementary data sets allow us to analyze the nanometer-scale magnetic and atomic correlations directly in real space, revealing the behaviors of paramagnons in a unique and intuitive way. The three-dimensional PDF reconstructed the MnTe atomic structure and visually showed that the magnetic correlations exhibit anisotropy, with longer correlation lengths along the crystallographic c axis than within the ab plane. The one-dimensional PDF confirmed and quantified these results, demonstrating that the enhancement to zT will be higher along the c axis where paramagnon drag is the strongest. Additionally, we present magnetic models in real space which reproduce the observed atomic and magnetic PDF patterns with quantitative accuracy. The significance of these results is discussed in the context of existing work on MnTe and other magnetically enhanced thermoelectric materials.

Keywords: Thermoelectric, Manganese Telluride, Spin Wave, Paramagnon, Neutron Scattering, Diffuse Scattering, Pair Distribution Function, Fourier, Anisotropy, Spin Correlation

ACKNOWLEDGMENTS

I would like to thank the Brigham Young University Physics and Astronomy department faculty who helped me learn the skills necessary for work on this thesis, as well as solidify my interest in studying physics. I would like to thank my advisor, Dr. Benjamin Frandsen, for helping me develop a passion for condensed matter physics. Without the opportunities Dr. Frandsen afforded me, this thesis and its content would not have been possible. His efforts helped me choose my future education and career path to be related to these subjects.

Contents

Table of Contents	iv
List of Figures	1
1 Introduction	3
1.1 Thermoelectric Materials and Manganese Telluride	3
1.2 Neutron Scattering	7
1.3 Pair Distribution Function Analysis	13
1.4 Goals	18
2 Methods	20
2.1 Experimental Methods/Procedure	20
2.1.1 Crystal and Powder Sample Fabrication	21
2.1.2 Neutron Diffraction Instrumentation	22
2.1.3 Sample Preparation and Data Collection	23
2.2 Computational Data Reduction and Analysis	26
2.2.1 Mantid Crystallographic Software	27
2.2.2 Three-Dimensional Pair Distribution Function Algorithms	28
2.2.3 Three-Dimensional Data Slicing and Visualization	29
2.2.4 One-Dimensional Pair Distribution Function with DIFFPY	30
3 Results	31
3.1 Neutron Scattering Experimental Results	31
3.1.1 Single-Crystal Diffraction Data	32
3.1.2 Powder Diffraction Data	32
3.2 Real-Space Magnetic and Atomic Correlation Analysis	35
3.2.1 Three-Dimensional Correlation Evaluation	35
3.2.2 One-Dimensional Correlation Evaluation	41
3.3 Challenges With Data Analysis	44
3.4 Conclusion and Future Work	48
Appendix A Visualization Package	53

Appendix B Punch-and-fill Method	58
Bibliography	61
Index	65

List of Figures

1.1	Visual representation of magnon and paramagnon drag	6
1.2	MnTe atomic and magnetic structure	8
1.3	Figures demonstrating how neutron diffraction occurs	10
1.4	Reciprocal lattice for MnTe hexagonal symmetry	11
1.5	Examples of designating planes using Miller indices	12
1.6	One-dimensional atomic pair distribution function simulated examples	15
1.7	One-dimensional magnetic pair distribution function simulated examples	16
1.8	Three-dimensional magnetic pair distribution function simulated examples	17
2.1	MnTe single-crystal used in neutron scattering experiment	21
2.2	Na-doped MnTe atomic and magnetic structure	22
2.3	Spallation Neutron Source instrument hall	23
2.4	Preparation of the MnTe single-crystal for the neutron scattering experiment	25
2.5	CORELLI tank used for injecting the single-crystal sample into the neutron beam-line	26
3.1	Examples of MnTe single-crystal neutron diffraction obtained at various temperatures	33
3.2	Examples of MnTe powder neutron diffraction obtained at various temperatures . . .	34
3.3	Isolated single-crystal diffuse magnetic scattering obtained at $T \sim 340$ K	36
3.4	Experimental and theoretical 3D- Δ mPDF calculated at $T \sim 340$ K	37

3.5	Linecuts demonstrating anisotropy in magnetic correlation lengths in paramagnetic state	39
3.6	Three-dimensional atomic PDF calculated for $T \sim 300$ K	41
3.7	Total 1D-PDF and isolated 1D-mPDF calculated at $T = 320$ K. Includes the extracted correlation lengths at various temperatures	42
3.8	Comparison of theoretical and experimental spin correlation functions	44
3.9	Elastic and inelastic single-crystal diffuse magnetic scattering and associated 3D- Δ mPDF obtained at $T \sim 340$ K	45
3.10	Linecuts taken through the $T \sim 340$ K scattering before and after Bragg peak removal	47
3.11	Elastic and inelastic single-crystal diffuse magnetic scattering and associated 3D- Δ mPDF obtained at $T \sim 370$ K	49
3.12	Elastic and inelastic single-crystal diffuse magnetic scattering and associated 3D- Δ mPDF obtained at $T \sim 415$ K	50
B.1	Elastic and inelastic single-crystal diffuse magnetic scattering and associated 3D- Δ mPDF obtained at $T \sim 370$ K, utilizing the punch-and-fill method	60

Chapter 1

Introduction

In this chapter, we describe the physics needed to understand the methods and results of this study. In Sec. 1.1, we explain how thermoelectric materials work and why they are useful for energy-related applications. The relevant characteristics of manganese telluride are explained in the context of paramagnon drag, a phenomenon through which magnetic correlations enhance an induced thermoelectric voltage. In Sec. 1.2, the physics of neutron scattering is explained. In Sec. 1.3, we give an introduction to real-space correlation evaluation through pair distribution function analysis.

1.1 Thermoelectric Materials and Manganese Telluride

Technological advancements made in the 21st century will largely be determined by our ability to address the energy and environmental challenges created by modern society. Innovations in materials science will play a critical role in this, with thermoelectric materials being one promising avenue for energy efficiency. Thermoelectric materials operate by the Seebeck effect, where a temperature gradient across a material can cause a voltage, or vice versa [1]. This effect allows thermoelectric materials to be used in a variety of environmentally friendly applications, including waste heat harvesting (such as converting car engine waste heat into usable energy) and solid state

refrigeration (advantageous due to the lack of moving parts needed).

The effectiveness of a thermoelectric material is quantified by zT , known as the thermoelectric figure of merit, a dimensionless number representing the maximum efficiency of energy conversion [2]. The thermoelectric figure of merit is defined as

$$zT = \frac{\sigma S^2 T}{\kappa} \quad (1.1)$$

where σ is the electrical conductivity (how easily a current flows through a material), S is the Seebeck coefficient (i.e. thermopower, governing the magnitude of an induced thermoelectric voltage), T is the temperature, and κ is the thermal conductivity (the rate of heat transfer in a material). Materials which can achieve a zT of at least 1 are generally considered to be high-performance thermoelectrics. Both σ and κ rely on the transport of electrons through a material, creating an interdependence that makes it difficult to increase zT beyond this threshold. The thermal conductivity κ also depends on phonons (vibrations in an atomic structure which propagate in a wave-like manner), but this varies from material to material. In metals, where electrons freely move around, κ has a stronger dependence on the transport of electrons over phonons, and thus correlates with σ —when one is increased, the other tends to increase as well. These effects cancel out in Eq. 1.1. In semiconductors, where electrons do not move as freely, κ will depend more strongly on phonons to transport heat, which decreases how much κ and σ compete with one another. The difficulty in increasing zT has resulted in a relative scarcity of high-performance thermoelectric materials which have practical application [3].

A material's magnetic structure provides an avenue to circumnavigating this problem. Just like vibrations can propagate through a lattice of atoms in wave-like fashion, so can disturbances in a material's magnetic structure. Each atom in a material contains a net magnetic moment caused by a quantum mechanical property known as spin. This allows an atom to act like a classic magnet with a north and south pole, characterized by both a direction and magnitude. The spins within a material will often have a preferred orientation which is driven by a system's desire to be in

the lowest energy state possible. The two kinds of spin configurations which are relevant to this paper are ferromagnetic (FM) and antiferromagnetic (AF) ordering. FM ordering is when spins tend to point parallel with each other, while AF ordering is when spins tend to point anti-parallel with each other. When the direction of a spin in a well-ordered configuration is perturbed by some means (such as by an external magnetic field), its deviation will influence the spins around it. Much like a domino effect, the initial disturbance propagates as a wave throughout the spin lattice, a phenomenon called a magnon (see Fig. 1.1). Through the transfer of linear momentum, a magnon can help drag electrons through the lattice, thus increasing the induced thermoelectric voltage across a material. This translates to an increase in the Seebeck coefficient S as seen in Eq. 1.1, making "magnon drag" appear to be an effective way to manipulate a material's thermoelectric properties [4–6].

Unfortunately, magnons are only defined for spin ordering which occurs over hundreds or thousands of unit cells of the material, known as long-range ordering. At high temperatures, where thermoelectric materials are most likely to be used, magnetic order tends to be weakened as thermal energy causes spins to become randomly aligned. It appears that this would severely limit the use of magnon drag. However, the concept of magnon drag is not reserved to only long-range ordering. Recent studies have shown that thermopower can be increased from short-range magnetic ordering as well, through a separate process known as "paramagnon drag" [6, 8]. Paramagnons, analogous to magnons, are thermal excitations which occur over short-range spin ordering present when a material has entered the paramagnetic state. This state is achieved when a material's temperature increases past its critical temperature T_C , a value marking where long-range magnetic ordering is lost but short-lived and short-range magnetic structures can still appear. The critical temperature for an antiferromagnetic material is known as the Neel temperature T_N . See Fig. 1.1 for a visual depiction of spin wave types. Paramagnons may be the key to magnetic enhancement of zT , as long as the local magnetic structures have sizes and lifetimes relatively large compared to the times and

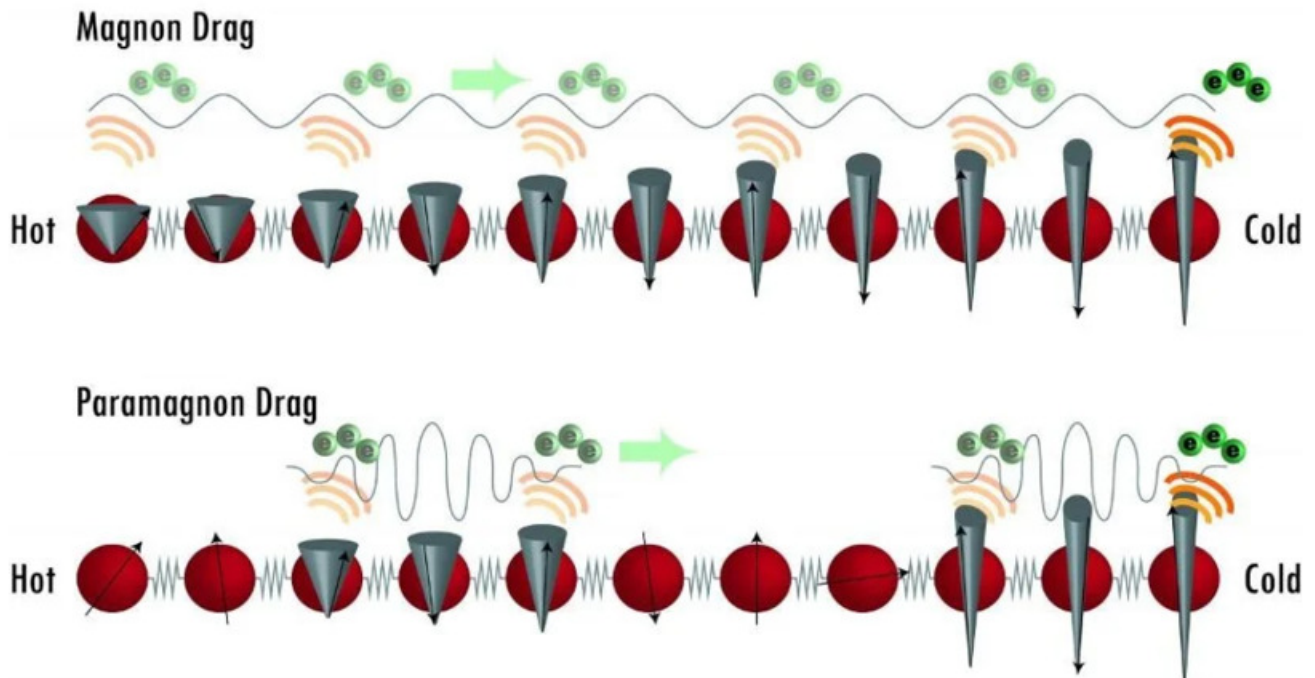


Figure 1.1 A visual aid to help understand the mechanism of paramagnon and magnon drag. The red spheres represent atoms, the black arrows represent spins, and the cones represent perturbations of these spins. The top spin chain shows the effects of magnon drag when a material is within the ordered state (temperature below T_N), where the spins are ordered over long distances. The perturbations of the spins propagate in a wave-like fashion, dragging electrons through the lattice. The bottom spin chain shows the effects of paramagnon drag when a material is within the paramagnetic state (temperature above T_N), where the spins are only ordered for a few atoms at a time. Paramagnons may appear like small magnon packets which can similarly drag electrons through the lattice. (Adapted from original image by Renee Ripley, Ohio State University [7])

lengths with which the paramagnon interacts with the electron. Under this condition, a paramagnon will appear indistinguishable from a magnon, resulting in a similar transport of electrons [6, 8].

The first material discovered to show an enhancement of thermopower through paramagnon drag was manganese telluride (MnTe) [8]. MnTe is a semiconductor with a hexagonal crystal structure, whose unit cell is shown in Fig. 1.2. The unit cell is the simplest portion of a crystal which still exhibits a repeating pattern, acting as the building block for the larger lattice. The three crystallographic axes, a , b , and c , are shown with directions, representing the edge lengths of the unit cell. The ground state of MnTe is classified as AF, seen by how the Mn^{2+} spins change directions along the c axis. Within the sheets formed by the a and b axes, the spins have FM ordering instead. MnTe has been shown to have a high thermoelectric figure of merit of $zT \approx 1$ at temperatures near 850 K, making it a candidate high-performance thermoelectric material. With a T_N of about 307 K, the regime where zT is large is well within the paramagnetic state; as such, magnon drag cannot be the source of the MnTe thermoelectric efficiency. Instead, there is strong theoretical and experimental evidence that this high zT value is due to paramagnon drag [8]. Despite our confidence in the contributions of paramagnon drag in MnTe, a clear picture of the short-range magnetic structure leading to the phenomenon is still lacking. Our objective is to study these short-range magnetic orderings to gain more insight into the nature of paramagnons in the paramagnetic state of MnTe using the experimental techniques of neutron scattering and pair distribution function analysis. These results may be used to inform future research concerning magnetically enhanced thermoelectric materials.

1.2 Neutron Scattering

One of the most effective experimental tools for probing a material's magnetic and atomic structure is neutron scattering. The process consists of passing a beam of neutrons through a sample and

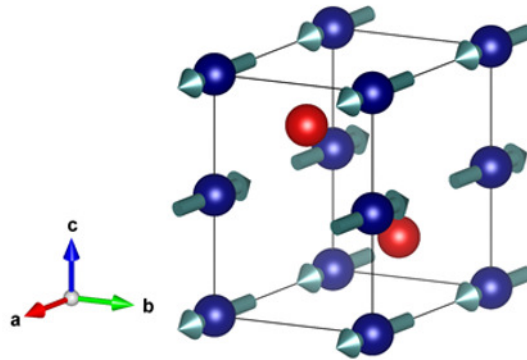


Figure 1.2 The unit cell of MnTe, showing its magnetic and atomic structure. The blue spheres are Mn^{2+} atoms with spin magnetic moments shown, while the red spheres are tellurium (Te) atoms. The Mn^{2+} spins have AF alignment along the c axis, and FM alignment within the ab plane. The unit cell parameters are defined to be $a = 4.193 \text{ \AA}$, $b = 4.193 \text{ \AA}$, and $c = 6.752 \text{ \AA}$.

measuring which angles the neutrons scatter into. Neutrons have neutral charge, so they do not interact with the charge of electrons, but they do interact with nuclei through the strong force, providing information about the arrangement of atoms in the material. Additionally, neutrons have a spin, which means they will interact with the magnetic fields present in a material. Matter containing unpaired electrons will have a net magnetic field due to the contributions from an electron's spin magnetic moment, and the neutron is a useful probe for determining how these spins tend to order themselves.

When neutrons enter a sample, information about a material's structure and dynamics are encoded in the details of how the neutrons scatter from the atoms and spins. If a neutron's kinetic energy is conserved upon scattering, we call this elastic scattering or neutron diffraction. This type of collision can be roughly visualized as the interaction between a ball launched at a rigid wall. The ball bounces off the wall with a change in momentum only by direction and not magnitude, since the wall is fixed. However, because the atoms and spins in a real material are free to move to some extent, a neutron's kinetic energy will often be changed upon scattering. This is defined as inelastic

scattering. An experimenter's goal is to often isolate the elastic scattering since it gives information only about the material's structure, while inelastic scattering gives information about how a neutron may exchange energy with the lattice, a process that lends insight into the dynamics of a material.

In addition to energy considerations, we can also categorize scattering by long-range and short-range ordering. Materials like MnTe have crystal structures, where atoms are well-organized into a repeating pattern over numerous repetitions. This long-range ordering results in elastic scattering patterns representing the material's average structuring. Many materials will also have short-range ordering which deviates from the average, such as one atom being substituted for another, missing atoms, and even disorder caused by thermal energy. Neutron scattering is powerful because it can help us detect both of these orderings. Long-range atomic and magnetic ordering manifests itself through Bragg scattering, as demonstrated in Fig. 1.3a. Bragg's law describes the conditions required for a wave to diffract constructively from the layers of a well-ordered lattice, and was first discovered through X-rays [9]. Due to the quantum mechanical concept of matter waves defined by the de Broglie wavelength ($\lambda = h/p$), subatomic particles such as the neutron can experience the same phenomenon. As long as a neutron's de Broglie wavelength is comparable in size to the distance between lattice layers, it diffracts in a similar manner to how light waves bend around obstacles. Short-range atomic and magnetic ordering manifests itself through diffuse scattering, defined as scattering resulting from deviations from the crystal structure. In other words, diffuse scattering encompasses any scattering that is not Bragg scattering. Diffuse scattering can be inelastic, unlike Bragg scattering, and is the key to studying the short-range ordering causing paramagnons in MnTe. Total scattering is defined as Bragg and diffuse scattering mixed together [10].

Upon diffracting with the lattice, a neutron experiences a change in momentum. According to the de Broglie relation, this change of momentum is related to a change in the k-vector, or wave number of the neutron. If we find the change in the k-vector given by the angle the neutron scatters into, we have effectively found the change in momentum of the neutron as demonstrated in Fig. 1.3b.

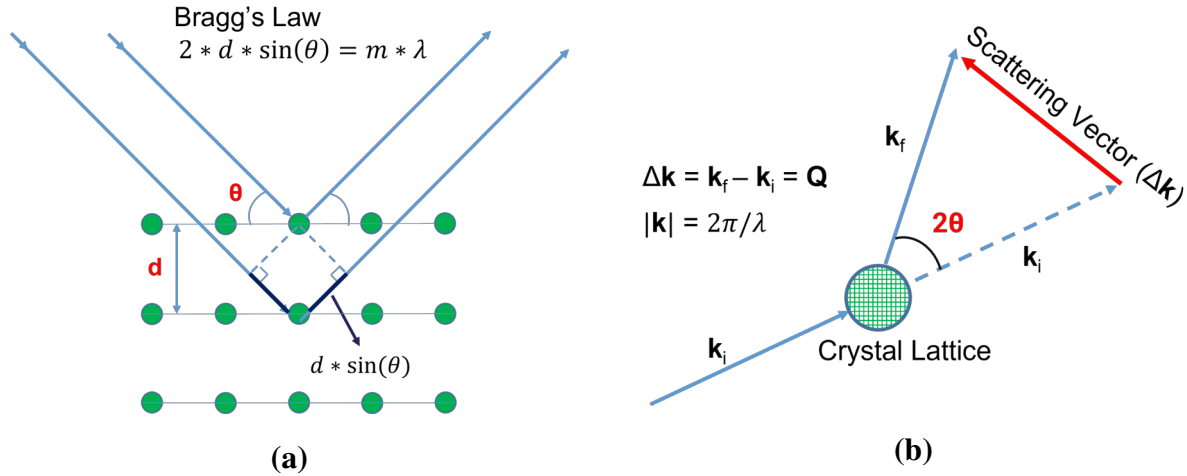


Figure 1.3 (a) Bragg's Law, describing how an incoming wavefront may interact constructively after diffracting from a lattice. (b) The change in \mathbf{k} -vector defines \mathbf{Q} -space (momentum space) where neutron diffraction is recorded. When scattering is elastic, $|\mathbf{k}_i| = |\mathbf{k}_f|$ and $|\mathbf{Q}| = 2 * |\mathbf{k}_i| * \sin(\theta)$.

This difference in \mathbf{k} -vector is defined as \mathbf{Q} in neutron sciences, a vector with magnitude in units of inverse angstroms. As such, \mathbf{Q} -space (the space spanned by vectors \mathbf{Q}) is the reciprocal of real space, and encodes all the information needed to map out the scattering structures. In \mathbf{Q} -space, Bragg scattering is recorded in highly localized repeating positions because length scales are inverted—the regular, long-range ordering found in a lattice becomes sharp features in reciprocal space called Bragg peaks. In contrast, diffuse scattering appears exactly as its name suggests; as extended, diffuse features interspersed among the Bragg peaks.

Bragg scattering is closely tied with a material's reciprocal lattice, which is a set of points in reciprocal space with periodic positions given by the momentum transfer shown in Fig. 1.3b. The reciprocal lattice is defined and constructed by the three reciprocal lattice parameters b_1 , b_2 , and b_3 , whose units are the inverse of the real-space lattice parameters a , b , and c . Figure 1.4 shows the equations for the reciprocal lattice vectors as well as the reciprocal lattice unit cell calculated for MnTe. In a typical scattering experiment, we will find Bragg peaks at locations given by the reciprocal lattice because these points are where the difference in \mathbf{k} -vector allows

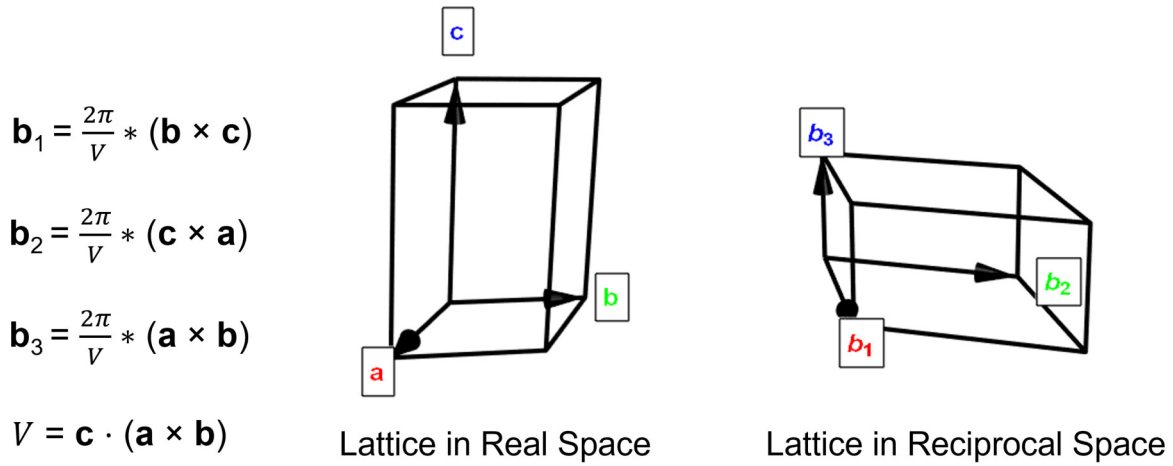


Figure 1.4 The reciprocal lattice and associated parameters b_1 , b_2 , and b_3 calculated from the MnTe unit cell. Because the reciprocal lattice vectors have inverse length units, the longer c crystallographic axis in real space becomes confined in reciprocal space. (Images created with Wolfram demonstration project "Crystal Lattices in Reciprocal Space" by Bianca Eifert [11])

constructive interference to occur. However, diffuse scattering cannot be predicted by a material's reciprocal lattice in the same way that Bragg scattering can be. Diffuse scattering happens because of impurities and deviations in a crystal's structure, resulting in patterns at places other than the reciprocal lattice points. A reciprocal lattice is an infinite and regular pattern, so it will only capture average behaviors and ignore any short-range ordering [10].

An alternative way to discuss locations in reciprocal space is through the Miller indices H , K , and L . The Miller indices are collectively a crystallographic notation which describes different lattice planes of the unit cell [12]. The indices themselves are proportional to the reciprocal of the unit cell parameters, meaning that one unit of H , K , or L is equal to $2\pi/a$, $2\pi/b$, or $2\pi/c$, respectively. Miller indices given in the form (HKL) represent the plane in real space that intercepts the three points a/H , b/K , and c/L of the unit cell. For instance, the point $H = 1$, $K = 0$, and $L = 0$ in reciprocal space, when written in the notation (100) , would represent the real-space plane with intercepts a , ∞ , and ∞ along the axes a , b , and c , respectively (infinity meaning the plane

1.3 Pair Distribution Function Analysis

Neutron scattering data can be difficult to intuitively understand in momentum space. The Pair Distribution Function (PDF) method aims to alleviate this by transforming neutron scattering data from momentum space to real space [10]. This transition is done through the Fourier transform, a technique often used in signal processing where the frequency domain representation of a dataset can be extracted. As a simple example, consider a sound wave recorded in time from a trumpet. This sound wave is composed of multiple different frequencies which are essential to know for an analysis of the trumpet's harmonics and tonal quality. The Fourier transform extracts the exact frequencies of this wave by transforming the data from the time domain to the frequency domain. Each frequency's amplitude and relative phase is also recorded, allowing for a full reconstruction of the wave. This method also works in reverse. If we instead started with measurements of the frequencies, amplitudes, and phases from a sound wave, we could Fourier transform the data to receive its full waveform in the time domain. The frequency domain of a sound wave is analogous to neutron scattering momentum space, which tells us the number of neutrons (amplitudes) which experienced a specific change in momentum (frequencies). Using the PDF method, we Fourier transform the neutron scattering into real space to give a more intuitive visualization of the structure of a sample, similar in idea to the waveform of the trumpet.

The PDF method is consistent with how we predict the positions of Bragg peaks from a diffraction experiment. Section 1.2 explained that the reciprocal lattice with imaginary points determined by constructive interference tells us the possible locations of Bragg peaks in the scattering signal. But how do we transform between the reciprocal and real-space lattices? The reciprocal lattice can be manually constructed by calculating the reciprocal lattice vectors using the equations in Fig 1.4 and translating the lattice points. However, we can also obtain the reciprocal lattice more gracefully through a Fourier transform of the positions of the atoms in a real-space lattice, which is exactly what the PDF method entails. And once again, this process is reversible; if

we instead start with a reciprocal lattice given by the Bragg peaks of an experiment, the PDF method (Fourier transform) will let us retrieve information about the average real-space ordering. It is important to remember that diffuse scattering results in signal at locations other than the reciprocal lattice points, so PDF analysis of diffuse scattering will give information about the deviations from the average real-space ordering.

Both one-dimensional PDF (1D-PDF) and three-dimensional PDF (3D-PDF) methods have been developed for neutron scattering, and either method can include magnetic and atomic contributions. If we Fourier transform the neutron scattering resulting only from the atoms and nuclei in a sample, then we obtain the atomic PDF which tells us about the placement of atoms in the lattice [13]. If we instead Fourier transform the neutron scattering from magnetic moments, then we obtain the magnetic PDF which tells us about both the placement of spins and their orientations in the lattice [10, 14, 15].

First we consider how to interpret the 1D atomic PDF. Atomic scattering appears as positive and negative peaks in the PDF pattern representing probabilities of finding pairs of atoms, also known as atomic correlations. The probabilities are weighted by the neutron scattering lengths of the atoms in the pair. Figure 1.6 demonstrates how an atomic PDF pattern can be deduced from a given lattice. Starting at an arbitrary atom within the lattice, the 1D atomic PDF considers radial distances as shown by the concentric circles in the figure. When another identical atom is found, a positive peak is recorded in real space at the radial distance between the pairing. If the pairing consists of two different atoms, then the 1D atomic PDF records a negative peak. Next we consider the interpretation of the 1D magnetic PDF (1D-mPDF), which is derived in a similar fashion but concerns magnetic (spin) correlations instead. Once again, we start with an arbitrary position of one of the atoms with its spin. When another spin is found at a certain radial distance away, the 1D-mPDF records a sign and strength of signal based on the relative orientation of the spins. If the spins tend to have a net FM ordering like the configuration shown in Fig. 1.7a, then the signal will be

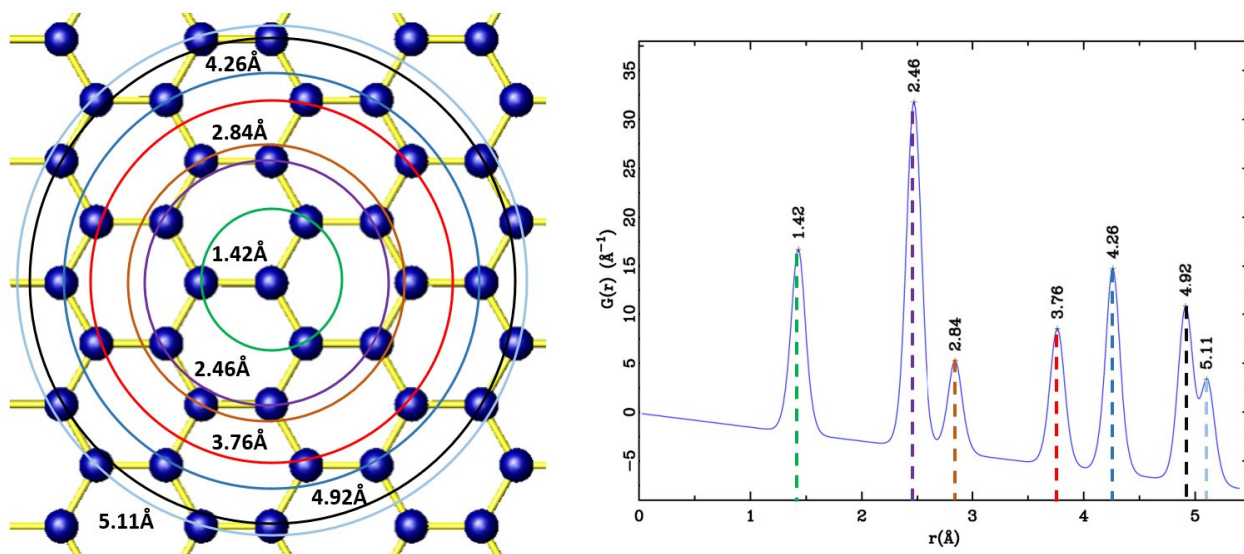


Figure 1.6 A visual demonstration of how to interpret an atomic PDF pattern. Each colored circle in the left figure represents a radial distance from an arbitrary atom where other atoms are found. The radii of the circles correspond to the color coded peaks in the right figure. Since all of the atoms are identical in this lattice, all of the atomic PDF peaks are positive.

positive. If the spins tend to have a net AF ordering like the configuration shown in Fig. 1.7b, then the signal will be negative. Finally, we can have a mix of positive and negative peaks if multiple spin pairings alternate between parallel and anti-parallel alignment, as seen in Fig. 1.7c. The strength of the signal depends on how strongly the pairings at a specific radial distance tend to point parallel or anti-parallel, meaning that spins pointing along the axis that joins them results in a weak signal in the 1D-mPDF.

One challenge of the 1D-PDF is peak overlap. Because the information recorded by this method is restricted to a single dimension, multiple atoms or spins can be found at the same radial distance from an arbitrary position and thus have their signals overlap with each other. This problem is largely eliminated by the spatial information given by the 3D-PDF. Interpreting the 3D-PDF is similar to the 1D-PDF; positive and negative peaks tell us the same information about atoms and spins, but instead of considering only the radial distance from an arbitrary point, we now consider

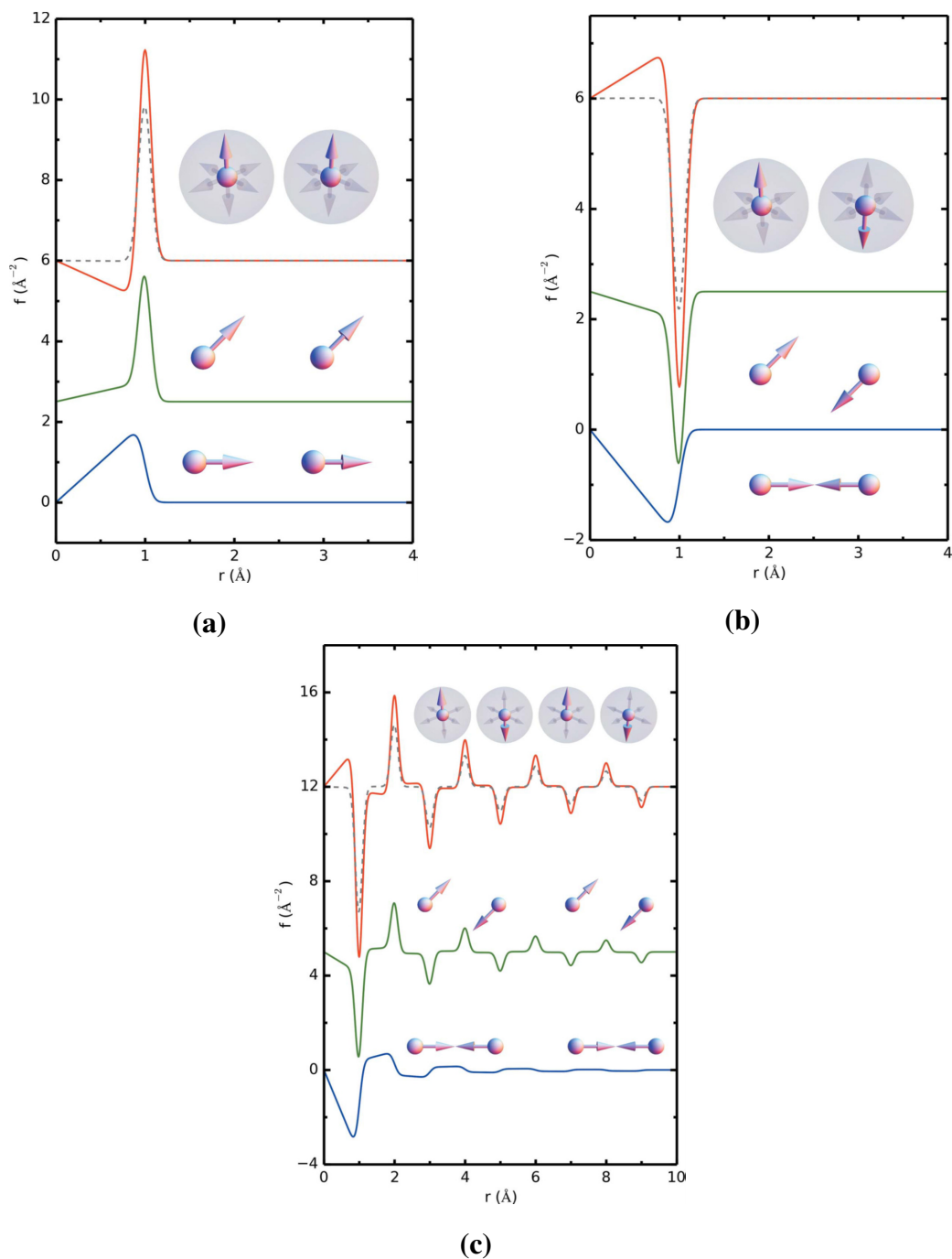


Figure 1.7 Source: figures 2, 3, and 4 from Frandsen et al. [14]. Demonstrates the expected 1D-mPDF patterns from different spin configurations. The 1D-mPDF signal is sensitive to the exact orientation of the spins, but has rotation invariance over the axis joining the spins. (a) Resulting 1D-mPDF from FM alignment of spins. (b) Resulting 1D-mPDF from AF alignment of spins. (c) Resulting 1D-mPDF from chain of alternating spins. The dashed line seen in all three panels represents averaging over all orientations while retaining the direction of ordering.

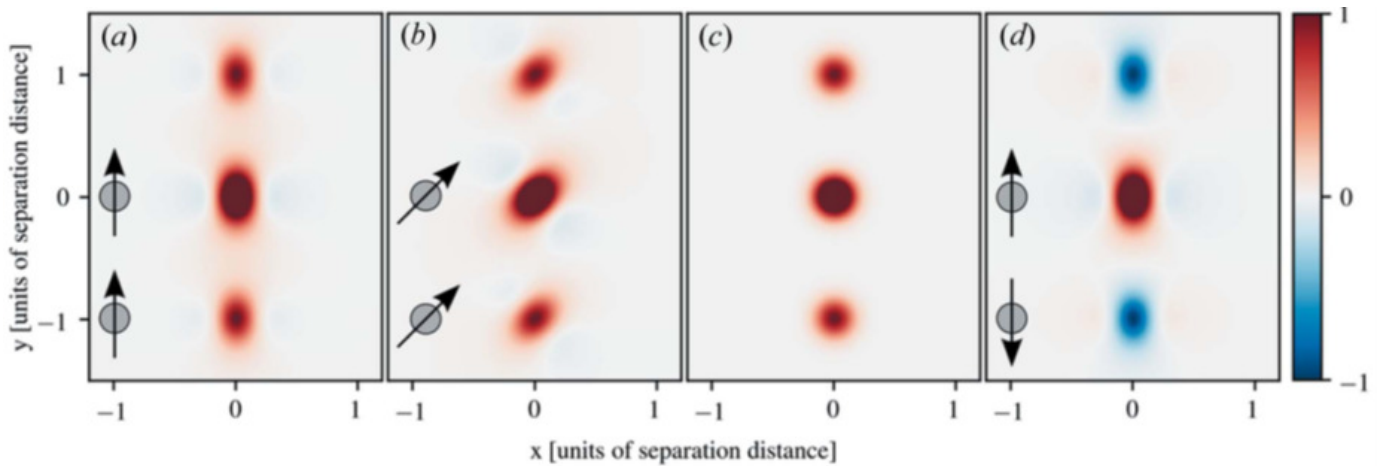


Figure 1.8 Source: upper panel from Fig. 1 of Roth et al. [16]. Demonstrates the expected 3D-mPDF patterns from different spin configurations. Each configuration has a positive peak at the center of the 3D-mPDF pattern because the spins have perfect FM alignment when shifted by the zero vector (a) Resulting 3D-mPDF from FM alignment of spins. Positive peaks are found at the separation vectors. Because a separation vector can start and end from either spin, two peaks are seen besides the center peak. (b) Demonstrates that the 3D-mPDF signal is sensitive to the exact orientation of the spins just as the 1D-mPDF shown in Fig. 1.7. (c) Resulting 3D-mPDF from averaging over all orientations. (d) Resulting 3D-mPDF from AF alignment of spins. Besides the positive center peak, negative peaks are found at the separation vectors.

three-dimensional separation vectors. Figure 1.8 shows the simulated 3D magnetic PDF (3D-mPDF) results we would expect from a few different spin configurations. Because the data received by the 3D-PDF is three-dimensional, visualizing the patterns requires projecting onto a 2D plane. To understand how the resulting pattern is obtained, imagine shifting the given spin configuration over itself with a separation vector. Whenever there is overlap of atoms or spins, a strong signal will be recorded in the 3D magnetic or atomic PDF at the position of the separation vector. Unlike the 1D-mPDF, the 3D-mPDF will record multiple peaks for a single spin pairing because separation vectors can point between the spins in either direction. This detail is important because it demonstrates how a 3D-PDF pattern does not result in a perfect map of the lattice from which it is derived. Instead, it tells us the nature of spin and atomic correlations.

As explained in Sec. 1.2, neutron scattering can occur from both long-range and short-range ordering. If we derive PDF from total scattering (containing both Bragg and diffuse), the features resulting from Bragg and diffuse scattering may overlap with each other, making it difficult to identify paramagnon behaviors based on short-range magnetic ordering. Therefore, it is imperative in our study that we isolate the diffuse scattering. The 3D-mPDF of isolated magnetic diffuse scattering is known as the three-dimensional magnetic difference pair distribution function (3D- Δ mPDF). If the isolation is done correctly, the 3D- Δ mPDF should only show short-range magnetic correlations representing deviations from the average structure. Above T_N , the average magnetic structure will be weak because the spins are in an uncorrelated state over long-range, resulting in strong signals from the 3D- Δ mPDF because short-range spin correlations still exist. Below T_N , the 3D- Δ mPDF would show weak signals because the spin structure should be strongly ordered in the configuration shown in Fig. 1.2, having very few deviations from the average.

1.4 Goals

Our primary objective is to provide a clear picture of the short-range magnetic correlations in MnTe through neutron scattering and PDF analysis. Understanding how spins tend to order themselves over short distances in the paramagnetic state of MnTe will clue us into the formation and behavior of paramagnons, short-range spin waves which drag electrons through the lattice, increasing zT . We also intend to provide additional support for the presence and relevancy of paramagnons in MnTe. We must show that the paramagnons are present at the temperatures where zT is large, despite the possibility of losing all correlations due to thermal energy. Finally, we hope to showcase the value of magnetic PDF techniques for probing short-range magnetic correlations, especially for those with an untrained eye for interpreting scattering data.

Now that the groundwork of physics has been laid out, a discussion of our neutron scattering

experiments on MnTe can begin. Chapter 2 will focus on the methods and procedures used to gather and analyze neutron scattering data, including instrumentation, software, and techniques for isolating diffuse scattering and PDF analysis. Chapter 3 will focus on the results of applying the principles outlined in chapter 2, discussing the implications of the presented data and suggesting future directions of work.

Chapter 2

Methods

In this chapter, our methods for collecting, reducing, and analyzing neutron scattering data are explained. In Sec. 2.1 we give brief overviews of how the neutron diffraction instrumentation operates, as well as how we prepared the samples for data collection. In Sec. 2.2 we describe how we used crystallographic software to combine, normalize, and fit our data along with the PDF algorithms used for real-space analysis. Additionally, our methods for visualizing three-dimensional data are presented.

2.1 Experimental Methods/Procedure

Here we discuss the nature of our single-crystal and powder samples of MnTe. We detail the process of preparing, mounting, and inserting the single-crystal sample into the neutron beamline. We identify the powder and single-crystal diffractometers used at the Spallation Neutron Source, and explain how a correlation chopper is able to distinguish between elastic and inelastic scattering. Finally, the steps carried out by the instrumentation for collecting the single-crystal neutron scattering data is presented.

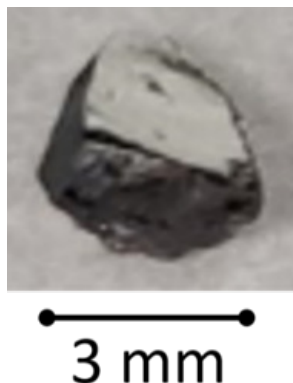


Figure 2.1 An image of the single-crystal MnTe sample used for experimentation.

2.1.1 Crystal and Powder Sample Fabrication

We prepared both single-crystal and powder samples of MnTe for experimentation, since the two forms of MnTe provide different kinds of data which are complementary. When neutrons are diffracted from a powder, the resulting patterns are one-dimensional due to the isotropic nature of the sample—that is, every crystalline orientation possible is equally represented in the powder. In contrast, a single-crystal specimen has a highly ordered crystal structure, so diffraction patterns provide three-dimensional structural details. The single-crystal sample consisted of pure MnTe, with a mass of 96.4 mg and dimensions of 3 mm on every side, as shown in Fig. 2.1. The single crystal was grown out of Te flux by keeping a mixture of Mn:Te = 36:64 at 890 C for 12 days. The powder samples consisted of both pure and 2% Na-doped MnTe. Doping, the process of introducing impurities into a material intentionally, was accomplished by mixing Mn powder, Te pieces and Na pieces in an argon glove box, sealing the mixture in an evacuated quartz vial, and holding it at 950 C for 6 hours. Then, the vial was cooled in cold water to 650 C and held for another 72 hours. After this treatment, the mixture was ground into a fine powder with a mortar and pestle. The unit cell of Na-doped MnTe is shown in Fig. 2.2.

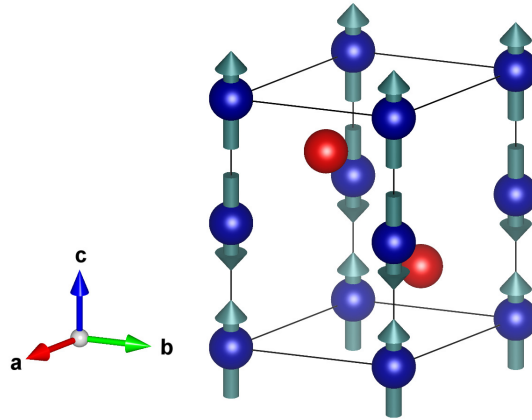


Figure 2.2 The unit cell of Na-Doped MnTe, showing its magnetic and atomic structure. The blue spheres are Mn²⁺ atoms with spin magnetic moments shown, while the red spheres are tellurium (Te) atoms. The Mn²⁺ spins have been reoriented to point along the *c* direction rather than in the *ab* plane, but the AF ordering is retained.

2.1.2 Neutron Diffraction Instrumentation

We conducted neutron scattering experiments on the samples of MnTe at the Spallation Neutron Source (SNS) at Oak Ridge National Laboratory located in Oak Ridge, Tennessee (Fig. 2.3). The SNS produces neutrons by accelerating protons into a mercury target, where the energy of the bombardment strips the mercury nuclei of neutrons in a process called spallation. These free neutrons are then directed down several beam-lines with different scattering instruments. For our single-crystal experiments, we used the CORELLI beam-line, or the Elastic Diffuse Scattering Spectrometer [17]. For our powder diffraction experiments, we use the NOMAD beam-line, or the Nanoscale-Ordered Materials Diffractometer [18]. Both instruments accept neutrons that are delivered in microsecond-long pulses with a spectrum of energies. As these pulses arrive at the sample within each instrument's chamber, the neutrons are scattered onto detectors which record impact positions and time-of-flight (an indirect measurement of energy).

The CORELLI instrument is able to distinguish between elastic and inelastic scattering. This energy discrimination is accomplished by the CORELLI correlation chopper, a rotating wheel made



Figure 2.3 A picture of the instrument hall at the SNS. The CORELLI instrumentation is housed inside the blue building, while the NOMAD instrumentation is in the rear of the facility (not visible in photo).

of carbon fiber and fitted with 255 open/closed elements randomly distributed around its perimeter. When operated asynchronously from the pulses, the correlation chopper modulates the beam by only allowing neutrons with certain energies to pass at certain times. The instrument records the chopper phase (where the wheel is currently at in its rotation) and time-of-flight associated with each neutron, allowing for reconstruction of the elastic scattering through cross-correlation methods. See [17] for more information on how the cross-correlation is used. Although the data collected from both the CORELLI and NOMAD instruments are complementary in our work, the bulk of this paper will focus on the methods and results associated with the single-crystal CORELLI experiment.

2.1.3 Sample Preparation and Data Collection

The single-crystal sample was prepared for experimentation by first being hand-mounted on a post using an epoxy adherent (Fig. 2.4a). The orientation of the crystal is important because it

determines the volume of reciprocal space obtained from the scattering. In this case, we mounted the crystal such that the H0L plane of reciprocal space coincided with the horizontal scattering plane. Aluminum foil was wrapped around both the sample and post to act as an anchor if the adherent were to fail (Fig. 2.4b). Scattering from the aluminum is a concern, so the foil was made thin enough to ensure that the neutron beam had little mass to interact with. Additionally, aluminum is adequately "transparent" to neutrons—that is, aluminum's neutron scattering cross section is small enough to allow neutrons to pass through with little interaction. To further limit the interference of scattering from anything but the crystal, a cadmium foil was wrapped around exposed parts of the mounting post to absorb incoming neutrons. The prepared sample was then attached to the end of a rotating rod (Fig. 2.4c) which was injected into the tank shown in Fig. 2.5. The chamber where the sample sits is filled with a helium exchange gas held at a pressure of a few millibars, allowing transfer of heat to the sample for testing at different temperatures.

Once in place, the sample was cooled down to a base temperature and data collection commenced. At each temperature, the sample was rotated through 360 degrees in steps of 3 degrees, resulting in 120 scattering patterns. This step size was chosen to account for the range in wavelengths of the incident neutrons ($\sim 0.64 - 2.86 \text{ \AA}$), allowing for continuous coverage of reciprocal space without any gaps. Each individual scattering pattern obtained was saved as both total scattering and elastic scattering versions. Upon completing 120 measurements, the sample was heated to the next target temperature to complete another full rotation, resulting in data at the temperatures of 6 K, 250 K, 330 K, 370 K, 400 K, and 445 K. It is important to note that these temperatures were measured by the instrument itself; due to limitations of precision at low pressure, along with a temperature gradient along the rod, they overshoot actual temperatures by as much as 30 K. Therefore, measurements we took at 330 K and 370 K are closer to 300 K and 340 K, respectively, lying below and above T_N . From now on in this thesis, the approximate actual temperatures will be used in place of instrument measurements.

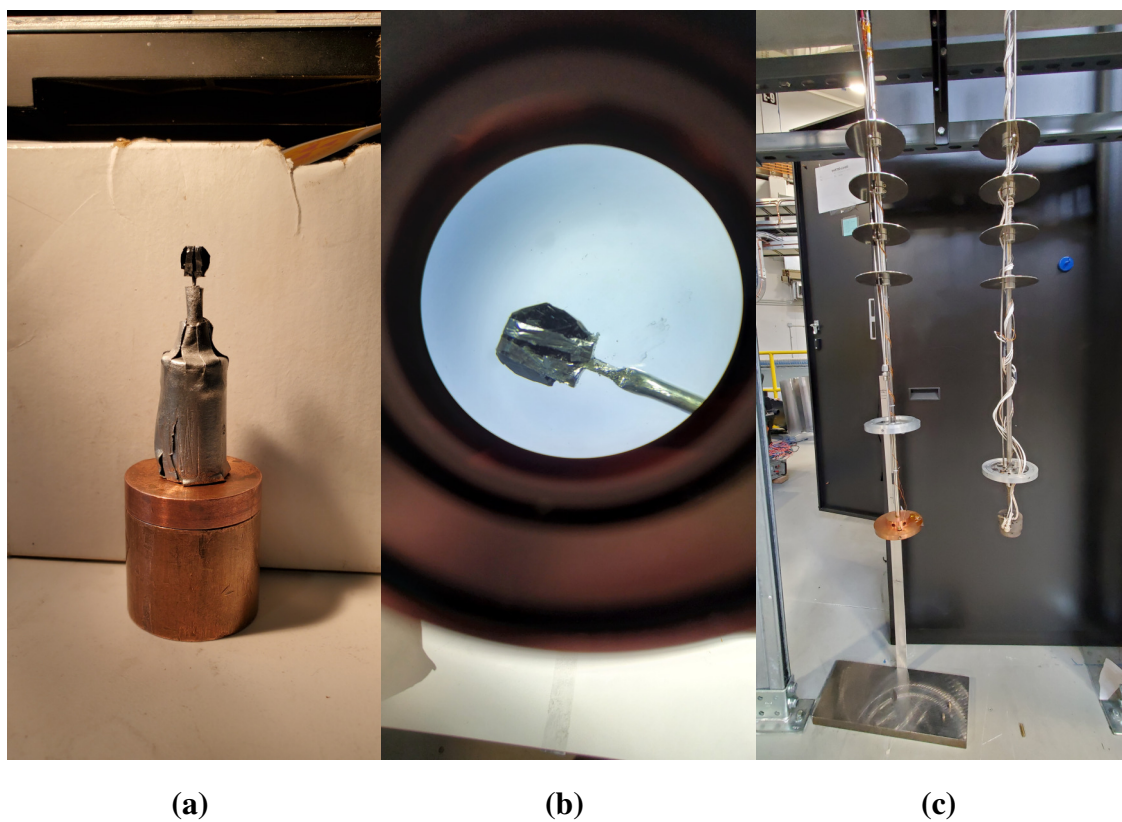


Figure 2.4 (a) Sample attached to the mounting post wrapped in cadmium. (b) Magnified view of the sample wrapped with aluminum foil. (c) The rods used to inject the sample into the beam-line and rotate the sample during the experiment. The mounting post shown in (a) is attached to the bottom end of these rods (where the bronze disk is seen).

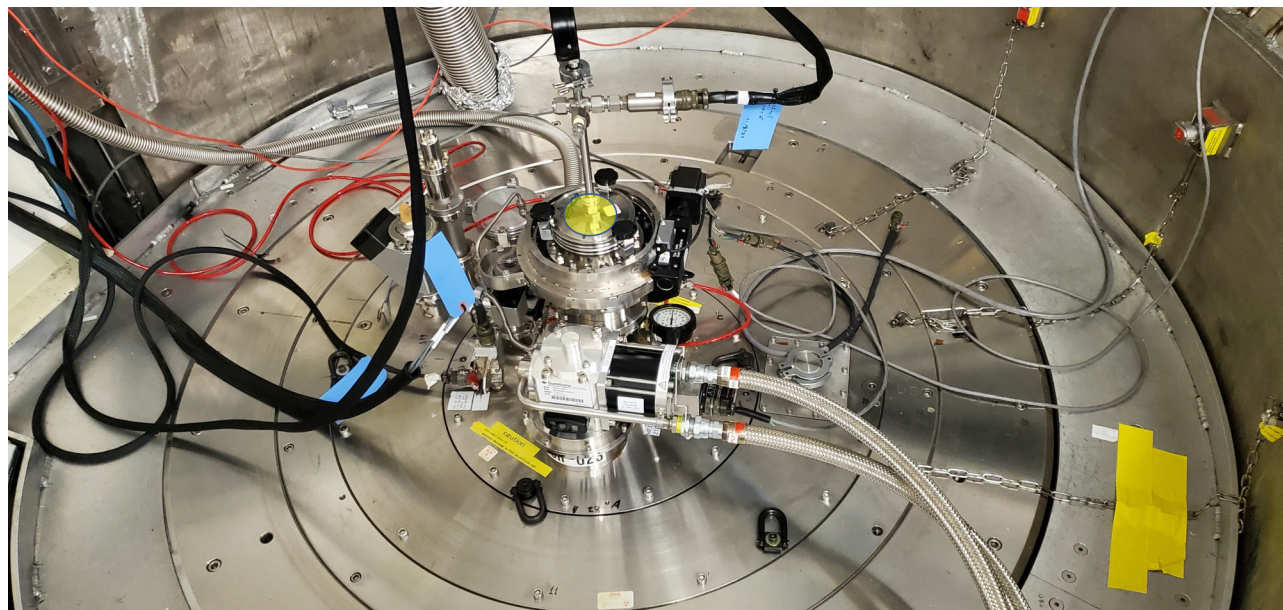


Figure 2.5 The tank where the sample is injected into the beam-line. The rod (Fig. 2.4c) is inserted through the top after the three black knobs are unscrewed, marked by a yellow circle over the image. The visible dial on the bottom right of where the rod is injected measures the pressure within the chamber.

2.2 Computational Data Reduction and Analysis

This section's purpose is to describe the tools we used to analyze experimental data. Mantid crystallographic software used for 3D data reduction, analysis, and visualization is presented, along with descriptions of 3D pair distribution function algorithms. Neutron scattering data is normalized using the MnTe crystal symmetry and a vanadium scattering reference. We explain how the KAREN and punch-and-fill methods provided by Mantid isolate diffuse scattering through Bragg peak removal. The process used to sequentially obtain the best 1D-mPDF fit through the `diffpy.mpdf` package is also briefly reviewed.

2.2.1 Mantid Crystallographic Software

The reduction and analysis of the diffraction data collected during the single-crystal experiment was done using Mantid crystallographic software [19]. A large international collaboration between several organizations including the SNS, the project provides a framework based on Python architecture for high-performance computing and visualization of neutron scattering data, including pair distribution function analysis. Data in Mantid is stored within a workspace as an event-based NeXus file, ready to be manipulated by the wide range of algorithms available to the user. Workspaces come in several forms based on the nature of the data and hold metadata such as specific instrument geometry, associated data errors, and workspace histories detailing which algorithms have acted on a particular workspace.

Once the data is obtained from the experiment it needs to be properly oriented and normalized to account for the sample's symmetry and instrument bias. All of this is done in Mantid. First, orientation matrices using the UB matrix formalism are created for each temperature (called the UB matrix for historical reasons, see [20]). These orientation matrices are determined by the positions of the diffraction peaks and are used to map the scattering angles obtained in the laboratory frame to the reciprocal lattice of the sample. For the normalization, each run at a particular temperature is loaded in along with a vanadium scattering reference and adjusted by the UB matrix. Vanadium results in a uniform, featureless incoherent scattering signal with no Bragg peaks, so it is useful for calibrating detector efficiencies and the instrument's solid angle (field-of-view of the detector). The individual runs are added together, divided by the vanadium scattering, and symmetrized according to the hexagonal structure of MnTe to obtain the final normalized signals. During the process, the user has the choice to isolate the elastic scattering by loading in the statistical chopper data, which then uses the elastic scattering patterns obtained at each temperature rather than the total scattering patterns.

2.2.2 Three-Dimensional Pair Distribution Function Algorithms

Mantid provides its own algorithm for 3D- Δ PDF calculations, called DeltaPDF3D. The algorithm utilizes the Fast Fourier Transform (FFT) from the Numpy library in Python to compute the discrete Fourier transform on the data we receive from our experiment. The algorithm takes binned data in reciprocal space as input with the requirement that the dimensions, called H, K, and L, be ordered as such. Our data was recorded with the order of the L and K dimensions flipped, so we transposed the data before sending it through the algorithm. Although DeltaPDF3D employs a window function to smooth out the edges of a scattering workspace before calculating the FFT, we still found an unacceptable amount of noise present in the resulting patterns. Therefore, we restricted the input scattering to a cube of reciprocal space with side lengths of approximately 18 \AA^{-1} by slicing off the ends of the data set. This does not exclude any meaningful scattering because the magnetic form factor suppresses scattering far away from the center of the Q-space. Care must be taken to slice each dimension of the scattering evenly because the DeltaPDF3D algorithm requires the data remain centered on zero.

In order to obtain the 3D- Δ mPDF, the diffuse magnetic scattering must be isolated from the Bragg peaks and any background signal found in the data. To do this, we subtracted data collected at a temperature below T_N from data collected above T_N , effectively removing the background signal. However, the subtraction on its own is not sufficient to remove the Bragg peaks. The DeltaPDF3D algorithm provides two different methods for removing these peaks: the punch-and-fill and KAREN [21] methods. The punch-and-fill method works by identifying locations of Bragg peaks based on unit cell parameters. Once found, these reflections are removed or “punched” out of the data using a sphere or cube with size determined by the user, leaving a hole. The DeltaPDF3D algorithm then fills in these holes with a smooth Gaussian convolution, which serves as an approximation to what the diffuse scattering around the peak would have looked like. The KAREN method, in contrast, does not require previous knowledge of the crystal’s parameters; instead, it employs a moving

window of defined width used to identify outliers in the data. When an outlier is found, it is removed and filled in by a value determined by the median of all values within the window. The more surgical procedure of the KAREN algorithm considers the possibility that diffuse scattering is not always approximated well by a Gaussian function. For this reason, we primarily used the KAREN method. Once reflection removal is completed by either of the two methods, an intermediate scattering pattern is created with the isolated diffuse scattering. This is the pattern used in the 3D- Δ mPDF calculation.

Despite the advantages of the KAREN algorithm, it presented a major challenge by often failing to fully remove a Bragg peak. The algorithm succeeds in scaling down and smoothing out the peaks, but the peaks remain partially intact even after several iterations of the KAREN algorithm is used on the same data. These signals are unwanted when calculating the 3D- Δ PDF since they may result in patterns from both long-range atomic and magnetic scattering, making it more difficult to identify short-range correlations. See Sec. 3.3 for evidence of this limitation.

2.2.3 Three-Dimensional Data Slicing and Visualization

The initial analysis of our single-crystal diffraction data was done in Mantid using the Slice Viewer tool, which provides an interactive 2D slice of the 3D data array. The Slice Viewer also allows for integrated line cuts to be taken through the data, projecting the signal onto a one-dimensional view useful for analyzing peaks. Despite its ease of use, the Slice Viewer is limited by only allowing slices to be taken along any of the three axes, making diagonal slices impossible. Additionally, there is no option for saving high-quality images of the slices in a format appropriate for publishing. For this reason, I developed a standalone Python Visualization package used for slicing through 3D data sets. By inputting the signal matrix, along with spatial arrays, a user can specify any size, resolution, and orientation of slice to be taken through the data. The slice is made by interpolation and then returned to the user as a 2D matrix, ready to be plotted as needed (see Appendix A for

code). The Visualization package is the primary way that we created figures of the 3D scattering and 3D-PDF patterns for presentations and publications.

2.2.4 One-Dimensional Pair Distribution Function with DIFFPY

We reduced the total neutron scattering data obtained from the powder samples using the NOMAD automatic data reduction scripts, setting a maximum extent in momentum space of $Q_{\max} = 25 \text{ \AA}^{-1}$. The experimental PDF were then obtained by Fourier transforming the normalized scattering data. Part of our powder diffraction analysis involved creating theoretical PDF fits to compare against the experimental PDF and validate our data. Our initial fits and analyses were done using PDFgui [22], a graphical interface which organizes fits and helps simplify plotting. PDFgui is available in the DIFFPY suite [23], a Python-based software for diffraction analysis. Our final fits were created through the `diffpy.mpdf` package, also included in DIFFPY, which allowed us to directly input magnetic structures and parameters to calculate theoretical magnetic PDF.

The procedure we followed to calculate the 1D-mPDF fits with `diffpy.mpdf` started with calculating an atomic PDF fit using the published atomic structure for MnTe [24]. We then subtracted this atomic PDF fit from the total experimental PDF data, leaving the mPDF signal and any imperfections introduced by the atomic PDF fit. In order to improve our fits by removing some of these imperfections, a second atomic PDF fit was calculated using the total PDF experimental data minus the mPDF signal we just isolated as the input data. This gives us an improvement over using only the atomic structure as a reference. The new atomic PDF fit is then subtracted from the original total PDF experimental data, giving us a second mPDF fit. This procedure was repeated once more to obtain a third and final mPDF fit with the most accuracy. Any subsequent repetitions of this process did not give any noticeable reduction in the residuals between the experimental and theoretical PDF.

Chapter 3

Results

In this chapter, we present the results from our neutron scattering experiments. In Sec. 3.1, we show the normalized 3D and 1D neutron scattering patterns. In Sec. 3.2, we conduct our short-range magnetic and atomic PDF analysis on both one and three-dimensional data, finding anisotropic correlation lengths which survive to high temperatures. Experimentally derived spin correlations and PDF calculations are shown to match theoretical predictions, lending legitimacy to our results. We conclude that paramagnons remain relevant in the temperature regime where MnTe achieves a high thermoelectric figure of merit, and that the enhancement to zT should be strongest along the crystallographic c axis. In Sec. 3.3, we describe the limitations of our methods based on experimental results. Finally, in Sec. 3.4 we discuss the possible directions for future work on MnTe and other magnetically enhanced thermoelectric materials.

3.1 Neutron Scattering Experimental Results

Here we present the normalized scattering data obtained from our single-crystal and powder neutron scattering experiments at the Spallation Neutron Source. We explain how short-range magnetic correlations are evidenced by the evolution of features as T_N is crossed. The probable causes of key

differences seen in elastic, inelastic, and doped MnTe scattering are identified.

3.1.1 Single-Crystal Diffraction Data

Most of our data analysis was done on scattering obtained at temperatures of approximately 300 K and 340 K, capturing both the ordered and paramagnetic state of MnTe since these two temperatures are below and above $T_N = 307$ K. Figure 3.1 shows the data gathered at ~ 300 K and ~ 340 K, comparing the elastic scattering (a, c) and inelastic scattering (b, d). The inelastic scattering was obtained by subtracting the elastic scattering from the total scattering. Interpretation of these figures is simple: any point where intensity is shown is a position in reciprocal space where a number of neutrons were detected. The larger the intensity of the signal, the more neutrons that were detected. The largest signals are found at the Bragg peaks, which appear as bright localized spots at regular intervals surrounded by diffuse scattering signal. Because the Bragg and diffuse scattering has not been separated in these patterns, the full extent of diffuse scattering is not shown. The difference in the scattering patterns between the elastic and inelastic data is attributed to scattering signals from phonons (lattice vibrations) and magnons (propagating spin waves) in the inelastic channel. By using the CORELLI correlation chopper's energy discrimination (as described in Sec. 2.1.2), these lattice vibrations and spin waves can be ignored, resulting in the elastic scattering. Both the inelastic and elastic scattering show rings of scattering intensity, which are a result of the aluminum sample holder as shown in Fig. 2.4b. Aluminum contains domains of well-ordered crystals, but is disordered over several crystals (polycrystalline), so scattering from it causes rings to appear rather than discrete spots.

3.1.2 Powder Diffraction Data

The powder diffraction data obtained for several temperatures for both pure and doped MnTe is shown in Fig. 3.2. The one-dimensional powder diffraction data has the advantage of clearly

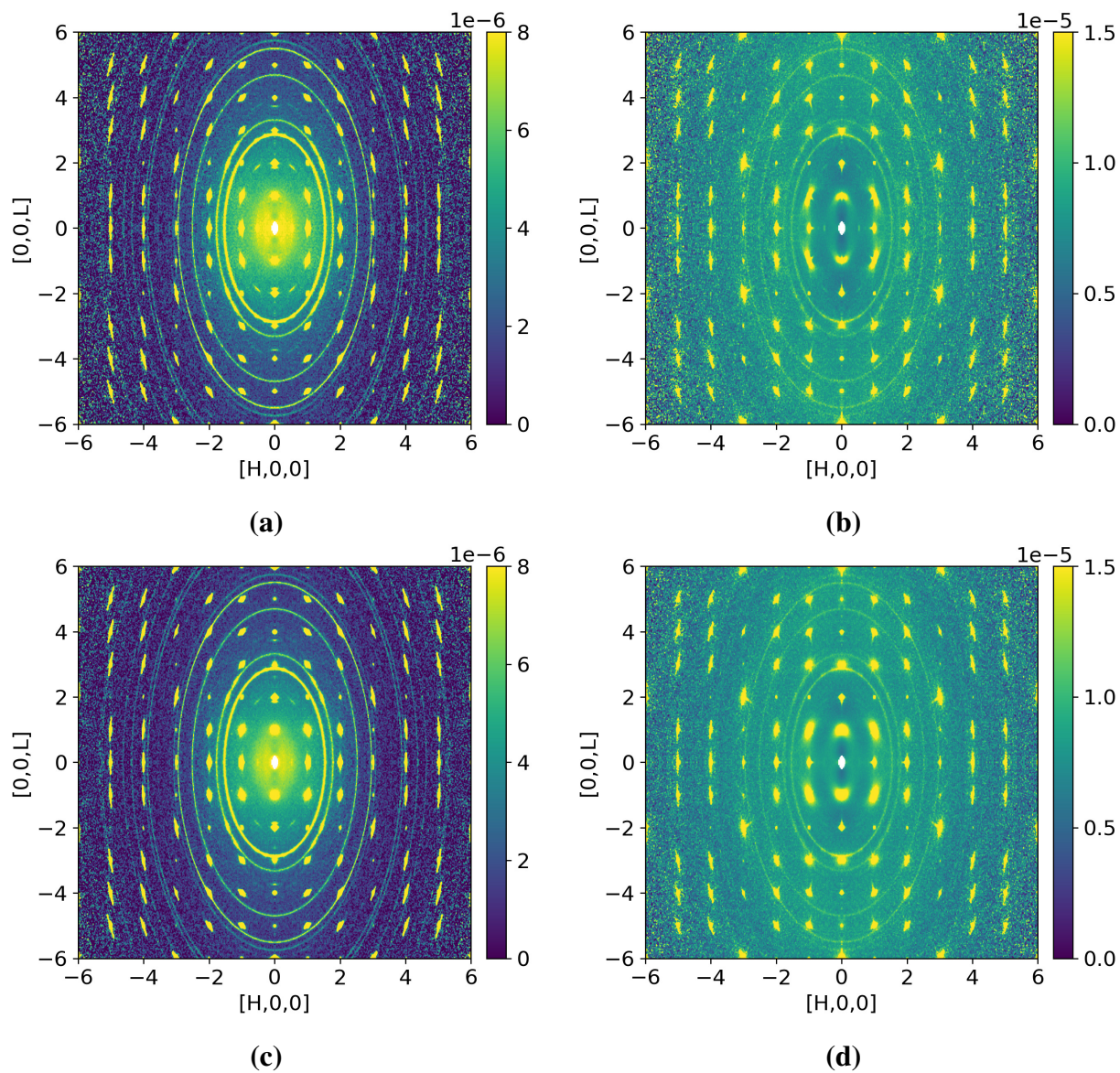


Figure 3.1 Neutron diffraction shown for the HOL plane. (a) Elastic at $T \sim 300$ K. (b) Inelastic at $T \sim 300$ K. (c) Elastic at $T \sim 340$ K. (d) Inelastic at $T \sim 340$ K.

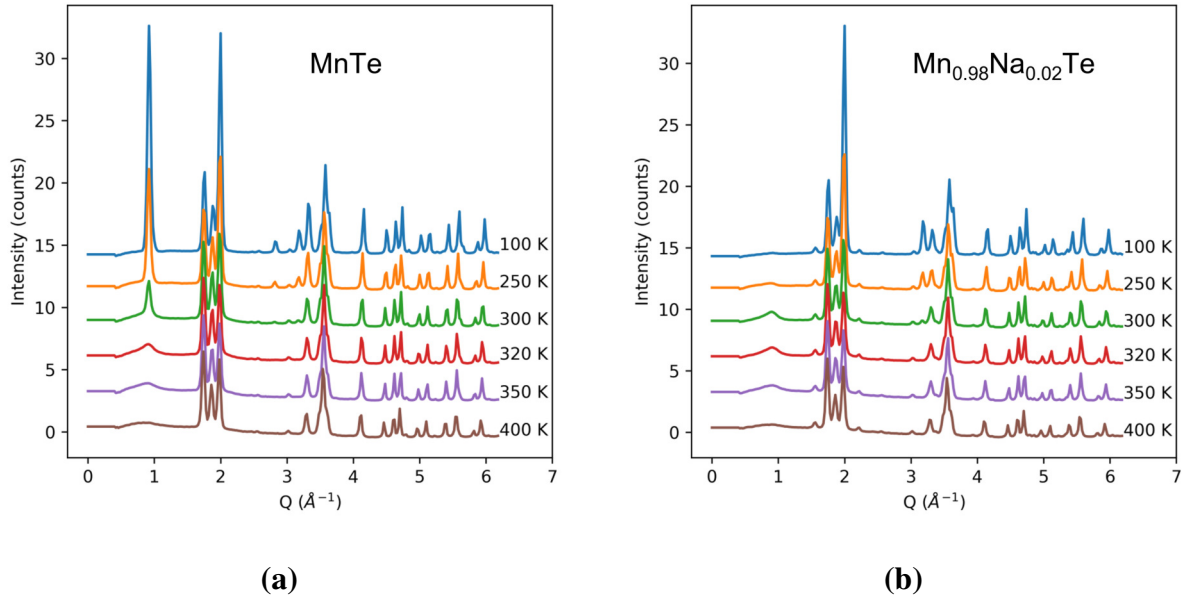


Figure 3.2 (a, b) Powder neutron diffraction curves for various temperatures for MnTe and Mn_{0.98}Na_{0.02}Te respectively.

showing us the magnetic transition in MnTe due to its simplicity compared to the three-dimensional crystal diffraction data. Well-defined magnetic Bragg peaks are found in the pure MnTe plot below the temperature of ordering around positions such as 0.9 \AA^{-1} and 1.9 \AA^{-1} (Fig. 3.2a). These peaks diminish in size as temperature increases, with an abrupt decrease when T_N is crossed. Afterwards, the sharp peaks become diffuse broad features, a sign of short-range magnetic correlations. The doped MnTe plot (Fig. 3.2b) is missing the large magnetic Bragg peaks at 0.9 \AA^{-1} , a result of the spins in the compound being reoriented to point along the c direction rather than in the ab plane as seen in Fig. 2.2. Despite the absence of the strong peaks, the doped MnTe data shares similar diffuse features with the pure MnTe data above T_N . These features are important to us because they indicate the possible presence of paramagnons.

3.2 Real-Space Magnetic and Atomic Correlation Analysis

In this section, the 3D-PDF and 1D-PDF are calculated and analyzed at multiple temperatures for insight into the MnTe magnetic and atomic correlations. The experimental PDF are compared to theoretical PDF fits to support our findings and identify possible anomalies. An analysis of 3D atomic PDF demonstrates how we can reconstruct an atomic lattice through neutron scattering. The 3D- Δ mPDF visually reveals anisotropic magnetic correlation lengths, with a longer correlation length along the crystallographic c axis than within the ab plane. The correlation lengths are quantified by extraction from the 1D-mPDF, showing a tendency for magnetic correlations to survive to high temperatures. This confirms the relevance of paramagnons in the temperature regime where the MnTe thermoelectric figure of merit becomes large. The shortcomings of the KAREN algorithm of Bragg peak removal are investigated, along with the challenges of our method for isolating diffuse scattering, demonstrating that these limitations may be the cause of warping effects seen in the experimental 3D-PDF. The breakdown of correlations by thermal scattering is demonstrated with higher temperature PDF calculations.

3.2.1 Three-Dimensional Correlation Evaluation

Analysis of the neutron diffraction and 3D- Δ mPDF gives us insight into the short-range magnetic correlations above T_N . The diffraction pattern shown in Fig. 3.3 was obtained at a temperature of ~ 340 K—this is an intermediate total scattering pattern viewed in the HOL plane after subtracting the 300 K data and removing the Bragg peaks. In this pattern, bright signals from diffuse scattering clearly remain around the original positions of the magnetic Bragg peaks, a good sign that our isolation method was a success. Additionally, the rings present in the normalized scattering are decreased in intensity from the subtraction, which helps eliminate the effects of noise in our subsequent PDF analysis.

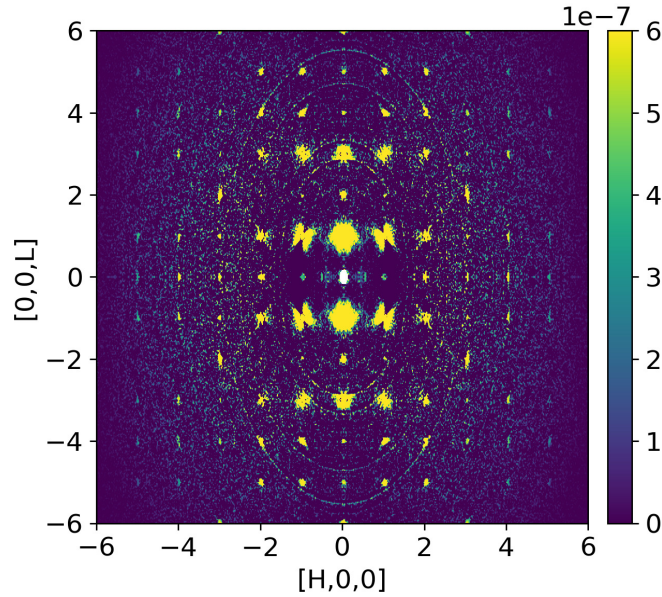


Figure 3.3 Diffuse magnetic scattering in MnTe at 340 K, shown for the H0L plane.

Figure 3.4a shows a slice of the 3D- Δ mPDF at ~ 340 K in the xz plane, where the a crystallographic direction is parallel to the horizontal axis, and the c crystallographic direction is parallel to the vertical axis. This 3D- Δ mPDF was obtained by passing the intermediate scattering shown in Fig. 3.3 through the DeltaPDF3D module in Mantid, providing us a real-space view of the short-range AF correlations present within the paramagnetic state of MnTe. As explained in Sec. 1.3, the orientation of spin pairs manifests themselves as positive and negative peaks in a magnetic PDF pattern; a positive peak represents FM alignment, while a negative peak represents AF alignment. The strength of the correlation is represented by the magnitude of these peaks. In this particular pattern, notice that the bright and dark regions alternate along the z axis, indicating that the spins in the c direction are antiferromagnetically ordered. Meanwhile, the horizontal direction exhibits rows with uniform color, indicative of FM alignment in the ab plane. Another visualization of this is shown in Fig. 3.4b, which displays the 3D- Δ mPDF pattern in the xy plane at $z = 0$. Here, the hexagonal structure of the MnTe unit cell can clearly be seen. The a and b axes are naturally non-orthogonal to each other due to the hexagonal symmetry, so one of these axes needed to be

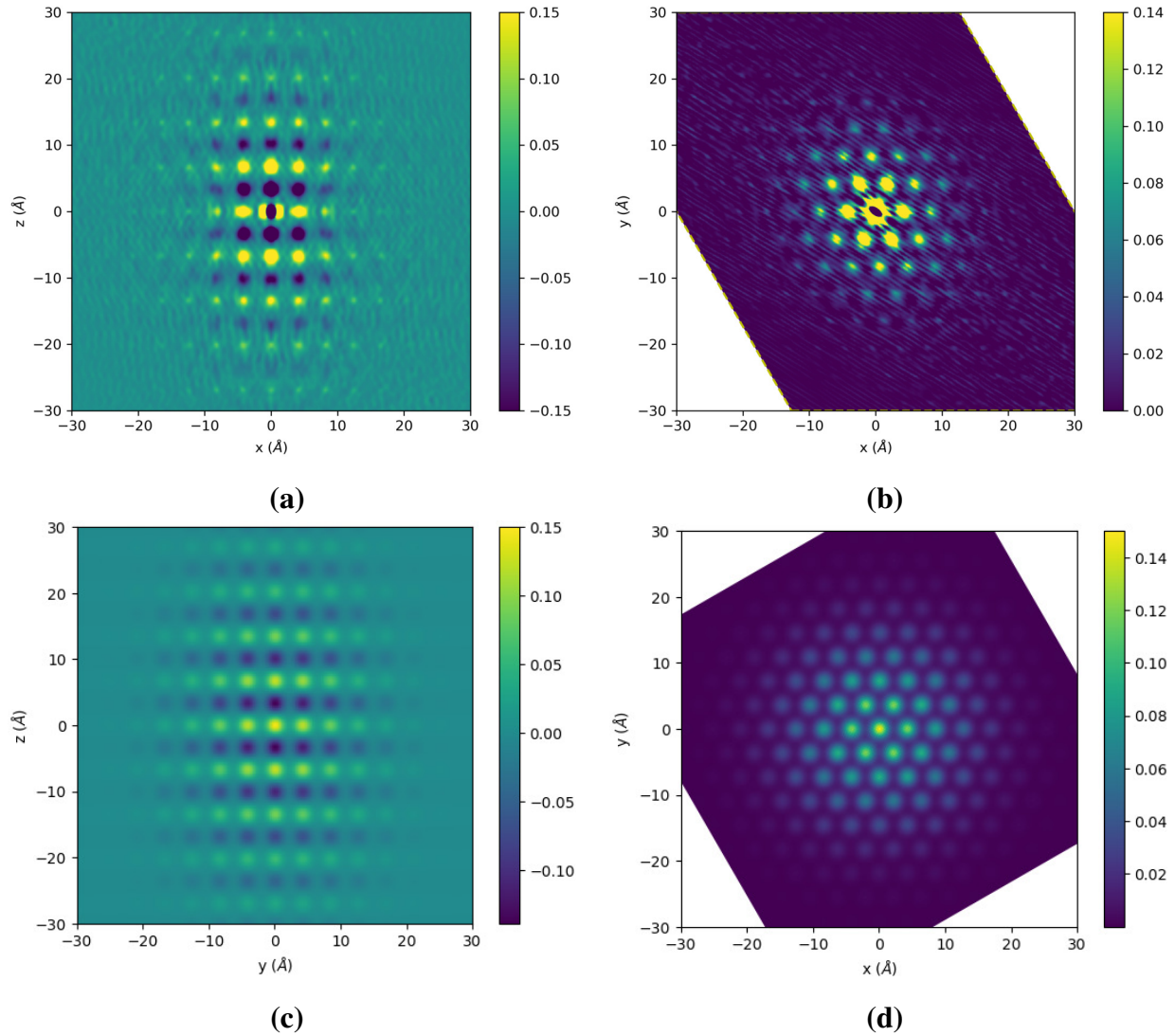


Figure 3.4 3D- Δ mPDF calculation at $T \sim 340$ K. (a) The experimental short-range AF correlations of MnTe in the xz plane where $y = 0$. (b) The experimental short-range FM correlations in the xy plane where $z = 0$. (c, d) Simulated short-range magnetic correlations of the yz and xy planes.

rotated by 120° to avoid warping the pattern. These figures together reveal that the planes alternate between uniform positive and negative peaks in $c/2$ steps along the z axis. This is consistent with the crystal and magnetic structure of MnTe shown in Fig. 1.2, where the spins are all aligned with each other in-plane (ab plane) but alternate in direction out-of-plane (c direction).

Besides confirming the MnTe spin structure, the patterns of Fig. 3.4 provide evidence of anisotropic correlation lengths, seen by how the bright and dark spots remain visible for a longer distance along the z axis than along the x or y axes. This can be quantified and visualized more easily by taking linecuts through the 3D- Δ mPDF along the $x = 0$ and $z = 0$ lines by projecting the signal down to a single dimension through integration, as seen in Fig. 3.5. Exponential envelopes are fitted to the peak profiles, giving us a correlation length of $7.7(4)$ Å for the z direction and a correlation length of $4.3(2)$ Å for the x direction. This anisotropy tells us that the ordering of spins in the paramagnetic state of MnTe is stronger along c , leading to a more pronounced paramagnon drag effect in this direction. As a result, thermoelectric devices utilizing MnTe would be able to maximize efficiency of energy transfer by orienting the material to operate along c .

With these quantified correlation lengths, a theoretical 3D- Δ mPDF was calculated for comparison to the experimental results, shown in Fig. 3.4(c,d). The model assumed a standard MnTe AF structure, built to match the structure in Fig. 1.2 while also incorporating the anisotropy we discovered experimentally. The calculations were done by a home-built extension of the `diffpy.mpdf` python package (courtesy of Parker Hamilton, graduate physics student at Brigham Young University), which calculates the 3D- Δ mPDF per the definition given by Roth et al. [16]. In short, the model works by using a vector autocorrelation of a given spin configuration. Each position in the 3D- Δ mPDF of Fig. 3.4(c,d) represents a separation vector which shifts the lattice of spins over itself. When this separation vector causes spins to overlap, a signal is recorded with strength based on the similarity between the orientations of the spins. This method allows deriving the 3D- Δ mPDF straight from the magnetic structure shown in Fig. 1.2, bypassing the need for obtaining scattering data and performing a Fourier transform. However, a theoretical model like this is unable to capture behavior such as anisotropy in correlation lengths, which is why the experimental data was needed prior to theoretical calculations. The validity of our experimental data is bolstered given that the experimental and theoretical PDF exhibit the same basic patterns. One important distinction is

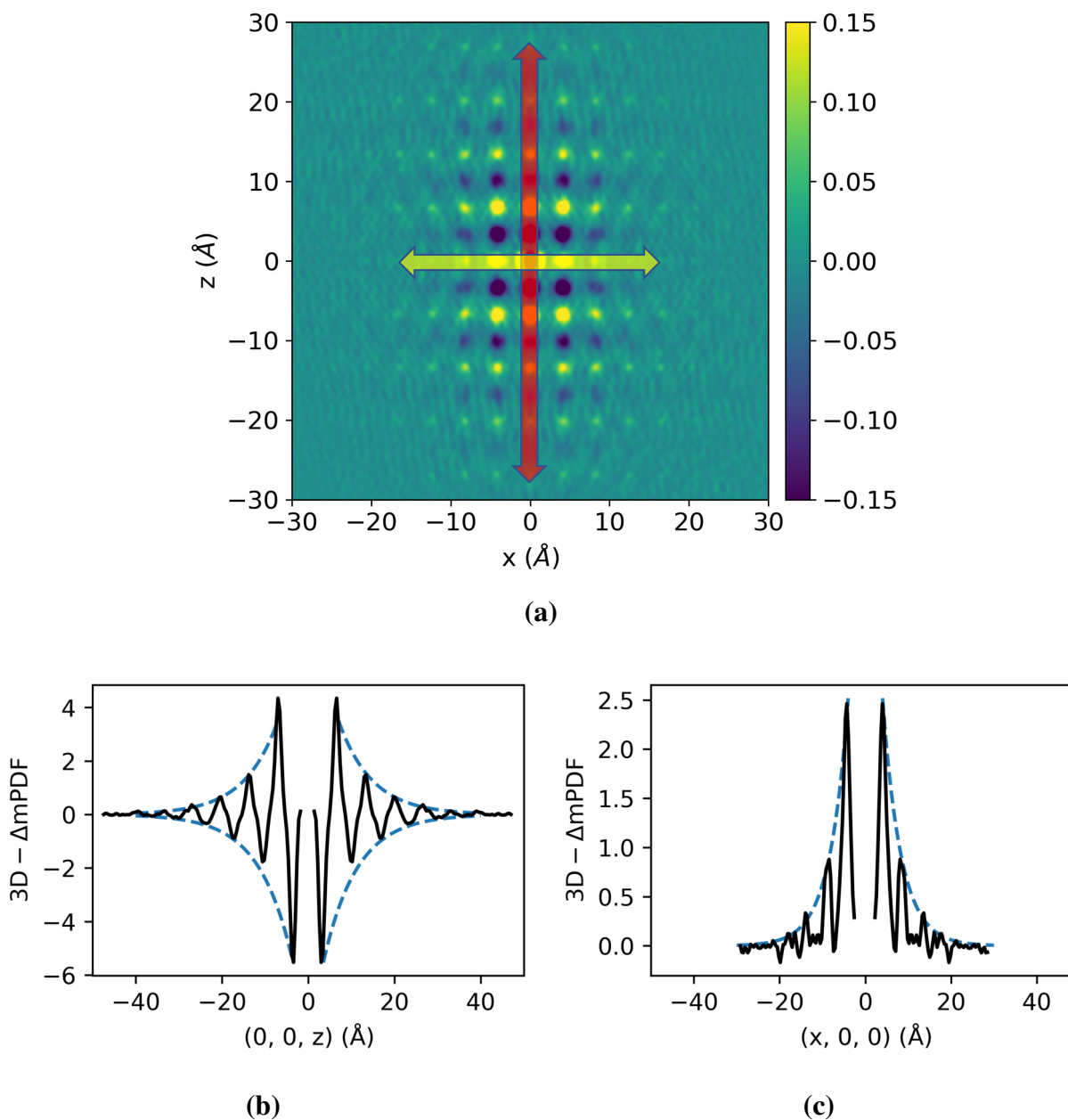


Figure 3.5 (a) Arrows overlaid on the 3D- Δm PDF as described in Fig 3.4a, demonstrating the difference in correlation lengths along the z -direction (red arrow) and x -direction (yellow arrow). (b) Linecut taken through the 3D- Δm PDF along the z direction with $x = y = 0$. The best-fit exponential envelope is shown by the dashed-lines, giving a correlation length of 7.7(4) Å. (c) Same as (b), but with the linecut taken along the x direction with $y = z = 0$, giving a correlation length of 4.3(2) Å.

the difference in the sign of the peak at the origin between the two patterns. The theoretical PDF has a positive peak at the origin, something we would predict since all spins perfectly align when the separation vector is the zero vector. The experimental PDF has a negative peak instead, which we attribute to noise in the data rather than a physically meaningful result. Another prominent difference is the warping effect on Fig. 3.4a, seen by the correlations which diminish in brightness along the x axis, not unlike hyperbolic functions in appearance. The effect is not seen in the theoretical pattern, and will be discussed in more detail later on in Sec. 3.3.

We can also examine the short-range atomic correlations using the PDF method. To do this, we need to remove all contributions given by both the Bragg peaks and magnetic scattering. We start with scattering obtained from below T_N , where MnTe is in the ordered state and all magnetic scattering is contained within the Bragg peaks. Therefore, removing the Bragg peaks with the DeltaPDF3D algorithm should also remove all magnetic scattering, leaving us with only the atomic diffuse scattering contributions. Figure 3.6 shows the results of this procedure for elastic scattering at $T \sim 300$ K. Important features to look for within the short-range atomic correlations are positive peaks surrounded by negative signal, and vice versa, indicating the possibility of an atom's tendency to displace itself from the regular position. Unfortunately, these kinds of interesting features do not show up in Fig. 3.6. It is possible that the features are too subtle to be detected over the noise in our data. However, we can at least confirm that the atomic correlations match with our MnTe unit cell. Looking at xz planes, we find that all the correlations are positive at integer values of b along the y axis (Fig. 3.6a), telling us that every atom within these planes are identical to one another. Then, at steps of $b/3$ along the y axis we find a more interesting pattern of alternating negative and positive peaks (Fig. 3.6b). This is consistent with the MnTe unit cell shown in Fig. 1.2, where the Te atoms (red) are found at a distance of $b/3$ and $2b/3$ away from the Mn^{+2} atoms in the ac plane, giving us the negative peaks in the pattern. The positive peaks are given by the two Te atoms paired with themselves. Here, a PDF pattern helped us reconstruct the exact atomic structure of MnTe. This is a

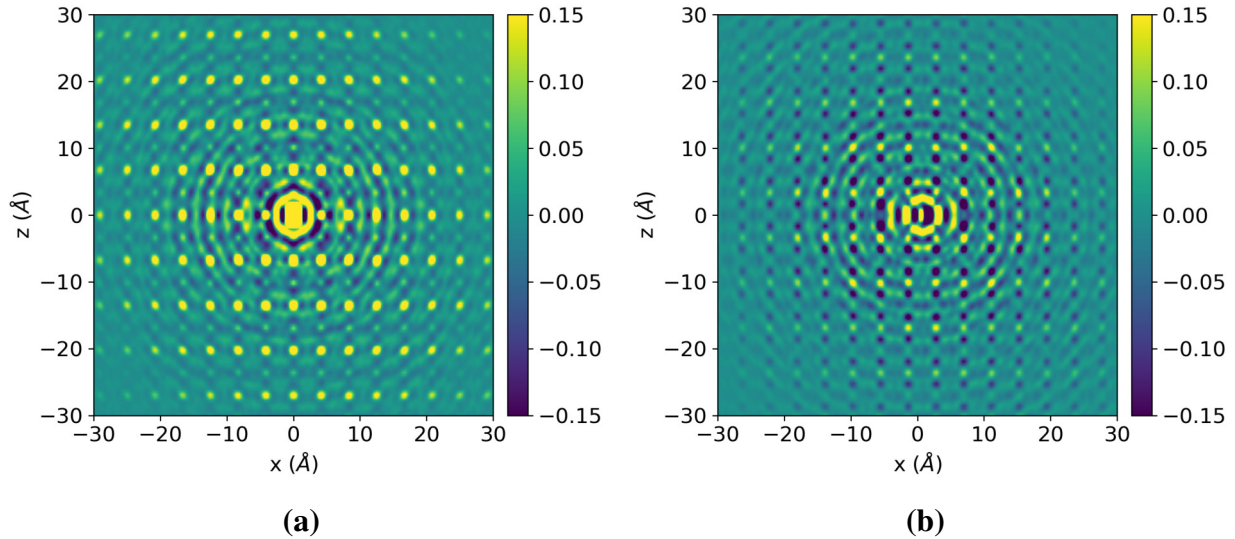


Figure 3.6 Three-dimensional atomic PDF calculated for $T \sim 300$ K. (a) slice in the xz plane where $y = 0$. (b) slice in the xz plane where $y = 1.3843$ Å, which is a third of a unit cell parameter in the b direction.

remarkable result; just like the magnetic PDF lets us visualize the magnetic correlations directly in real space starting with a diffraction pattern, so does the atomic PDF let us visualize the atomic correlations.

3.2.2 One-Dimensional Correlation Evaluation

The 1D-PDF of MnTe obtained from the powder diffraction experiments support the features we find in the 3D-PDF. Figure 3.7a shows the PDF obtained for MnTe at 320 K. Interpretation of the 1D-PDF is similar to the 3D-PDF; the peaks represent atomic and magnetic correlations found at some radial distance from any one atom. In the atomic 1D-PDF, positive peaks are pairings of identical atoms, while negative peaks are pairings of different atoms. In the magnetic 1D-PDF, positive peaks represent FM spin pairs, while negative peaks represent AF spin pairs. On its own, the 1D-mPDF is difficult to decipher visually, but we can still extract information such as the magnetic correlation lengths. Figure 3.7b is the result of making additional PDF fits to the powder

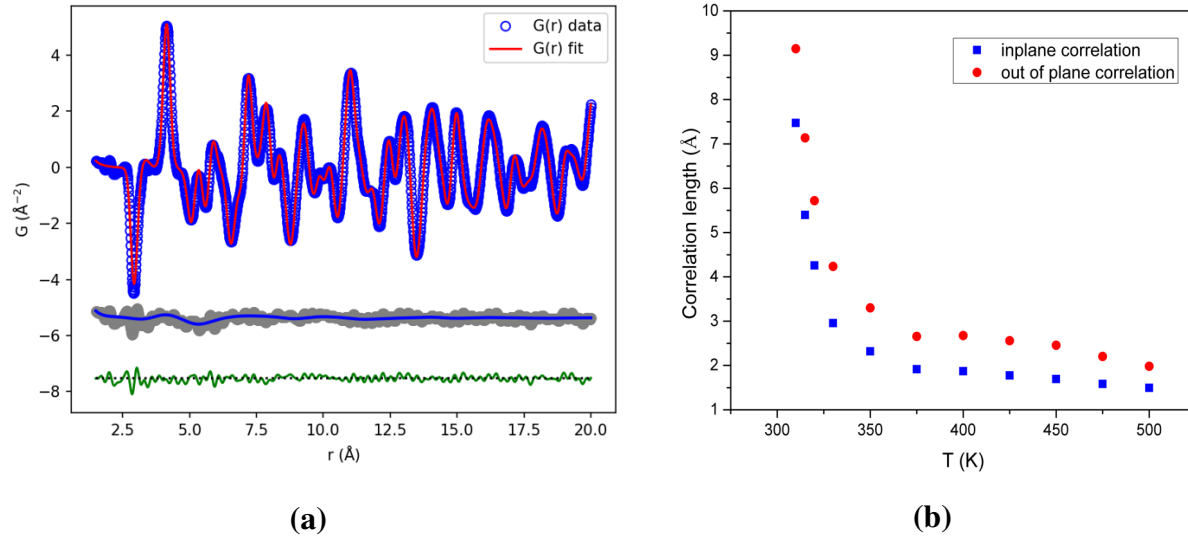


Figure 3.7 (a) Combined atomic and magnetic PDF fit for MnTe at 320 K, with the short-range AF correlations evidenced in the mPDF data (gray curve). (b) Temperature dependence of the best-fit correlation length along c (red circles) and within the ab plane (blue squares) in the paramagnetic regime, obtained from fits over 1.5 - 20 Å.

data at temperatures well beyond 320 K over a range of 1.5 - 20 Å. By allowing the models to have distinct correlation lengths along the c direction and within the ab plane, we were able to extract best fit values to demonstrate the anisotropy we see in the 3D- Δ mPDF. For all temperatures tested, the out-of-plane correlation lengths (red dots) were consistently about 50 percent larger in size than the in-plane correlation lengths (blue dots). This matched what we see visually in the 3D- Δ mPDF. Additionally, Fig. 3.7(b) shows that both correlation lengths experience a sharp drop up until about 350 K, but afterwards they stay relatively stable up to our highest temperature tested, 500 K. Based on the stability lasting for a large range of temperatures, it is highly probable that the correlation lengths should remain more-or-less constant at elevated temperatures beyond the ones tested here. This means that short-range ordering should be present at the temperatures where MnTe attains a high zT value, confirming the presence and contributions of paramagnons. The preservation of anisotropy tells us that the paramagnon drag enhancement of zT should be strongest along the c axis, even at high temperatures where thermoelectric materials are typically used.

The magnetic anisotropy in MnTe can be viewed as a result of the difference in strength of the exchange interactions along different directions. The exchange interaction is a way to quantify the strength and orientation that spins tend to align with; it is a quantum mechanical effect resulting from the symmetry requirements of overlapping wave functions. A positive exchange interaction means that it is energetically favorable for spins to align parallel, while a negative value means spins tend to be anti-parallel. Previously acquired inelastic neutron scattering data and calculations have found that the out-of-plane exchange interaction of MnTe is $J_1 = -21.5$ K, while the in-plane interaction is $J_2 = 0.7$ K [24, 25]. The signs of these values confirm that spins should have AF alignment along c , and FM alignment within the ab plane. The relative strength of the out-of-plane value compared to the weaker in-plane value tells us that spins will align with more strength along the c axis, supporting the anisotropy we have found experimentally.

The 1D-PDF results can be compared to theoretical predictions, just like we did with the 3D-PDF. Using the DLM-DFT-SIC approach [26], we were able to calculate the correlation function $\langle \mathbf{S}_0 \cdot \mathbf{S}_n \rangle$ for the first 9 nearest neighbors, where \mathbf{S}_0 is some arbitrary spin and \mathbf{S}_n is the n^{th} nearest neighbor spin. This correlation function is simply an inner product, calculating the strength and orientation of a correlation; positive and negative values correspond to FM and AF spin pairings, respectively. Figure 3.8 shows these correlation function values. At higher temperatures (beyond $T \sim 350$ K), the experimental and theoretical results remarkably agree with one another, giving legitimacy to our experimental data. At lower temperatures, the agreement breaks down, but the experimental results still identify the correct sign for the correlations. Fortunately, thermoelectric applications are usually done in the high temperature regime, so the agreement here demonstrates that we have an accurate, first-principles model of MnTe. This model can help us conduct future theoretical investigations of paramagnons in MnTe, even without any experimental data available.

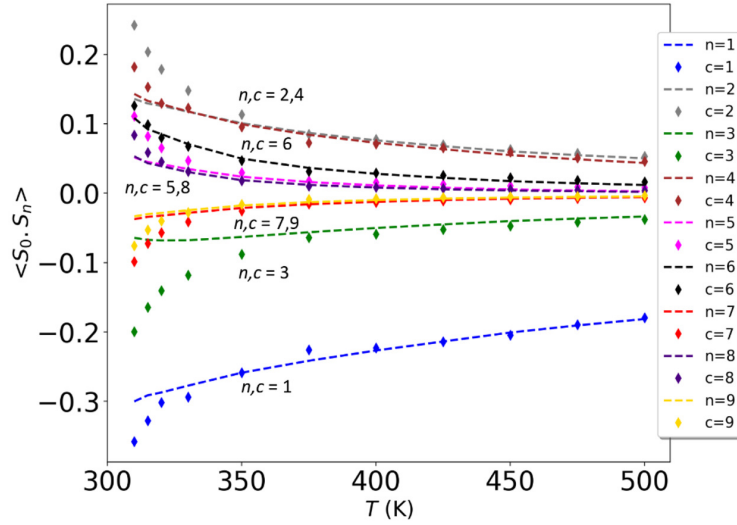


Figure 3.8 Theoretical (dashed lines) and experimental (diamonds) spin correlation functions $\langle S_0 \cdot S_n \rangle$ versus temperature for the first 9 nearest neighbor spins.

3.3 Challenges With Data Analysis

The method we used for isolating diffuse scattering was not without its challenges. For instance, oversubtraction causes the “butterfly” formations seen in multiple figures such as Fig. 3.3, with one located at $H = 1, K = 0, L = 1$. These features reveal that the scattering below T_N has a stronger signal in a ring intersecting the positions of some of the Bragg peaks. Although we do not currently understand the cause of this excess signal, we can identify its warping effects in our calculated PDF. First, we note that the 3D- Δ mPDF pattern of Fig. 3.4(a,b) was collected without any energy discrimination on the instrument, which means that it probes both the elastic and inelastic scattering contributions. By starting with the normalized elastic scattering, we can derive PDF which ignore the effects of lattice vibrations, as shown in Fig. 3.9. Figure 3.9c shows that the inelastic intermediate scattering contains pronounced butterfly features, while the elastic intermediate scattering of Fig. 3.9a does not. Then, the 3D- Δ mPDF for the inelastic scattering shown in Fig. 3.9d exhibits a pinching effect on the visibility of its correlations, giving the overall pattern a peanut shape, while the elastic 3D- Δ mPDF shown in Fig. 3.9b does not show this effect.

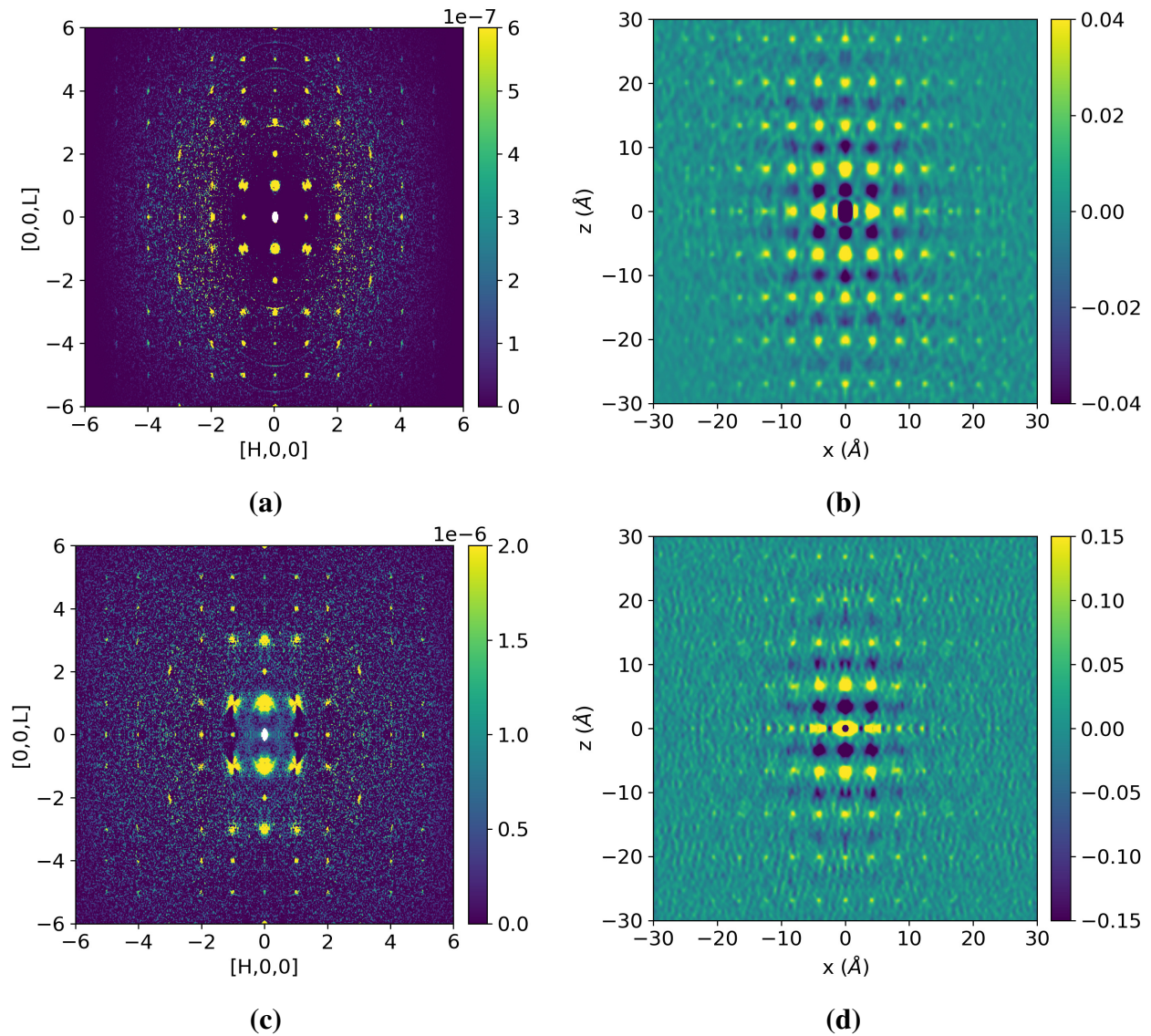


Figure 3.9 (a, c) Intermediate scattering (post subtraction and peak removal) at 340 K in the $H0L$ plane for elastic and inelastic scattering, respectively. (b, d) 3D- Δm PDF at 340 K in the $(x, 0, z)$ plane for elastic and inelastic scattering, respectively.

This suggests that the pinching in the calculated PDF is tied to the prominence of the wedges. This is supported by the theoretical 3D- Δm PDF (Fig. 3.4(c,d)) which lacks the warping effect since its calculation did not rely on our method of isolating diffuse scattering. We are currently investigating why the prominence of the butterfly formations differ between elastic and inelastic scattering.

As discussed earlier in Sec. 2.2.2, the use of KAREN also presents the challenge of Bragg peak removal. To demonstrate how KAREN fails to fully remove Bragg peaks, we took linecuts through the positions of some of the Bragg peaks for elastic scattering at 340 K, both before and after KAREN. The results for scattering with no subtraction is shown in Fig. 3.10(a,b). Notice that the peaks, although diminished in size, still remain sharp and prominent after KAREN is used, which is unlike how diffuse scattering would appear. The results for scattering with 300 K data subtracted from 340 K data are shown in Fig. 3.10(c,d), where the Bragg peaks start out as negative due to over-subtraction. For this scattering, KAREN is able to fill in the negative peaks with positive signal, and does a better job of decreasing the size of the peaks. However, sharp peaking does still remain, and subsequent applications of KAREN only serve to slightly reduce and smooth out the peaks each time. In order to fully isolate the diffuse magnetic scattering, the Bragg scattering contributions need to be fully removed, so the KAREN algorithm's inability to do this may introduce some uncertainty in our 3D- Δ mPDF results. We do not know the full implications of this issue, so future investigations could include a comparison between the PDF obtained while using KAREN and PDF obtained using an unrelated Bragg peak removal method. We would be able to identify how the limitations of KAREN manifest themselves in the resulting PDF patterns. As an aside, these linecuts are good evidence that our subtraction eliminates much of the background noise in the scattering data. Figure 3.10d is missing the rising and falling baseline seen in Fig. 3.10b. Additionally, the small peaks seen in Fig. 3.10b between $H = -2$ and $H = -1$, as well as between $H = 1$ and $H = 2$, are removed during subtraction. These are two of the bright rings found in the normalized scattering of Fig. 3.1, which were identified as scattering from the aluminum sample holder.

Most of our data analysis was done on temperatures near T_N and below it. Besides the transition at T_N being important to our research question, this is also because of the increasing effects of thermal scattering as the temperature of scattering increases. Figure 3.11 shows the intermediate scattering received by subtracting 300 K data from $T \sim 370$ K, along with the calculated 3D- Δ mPDF.

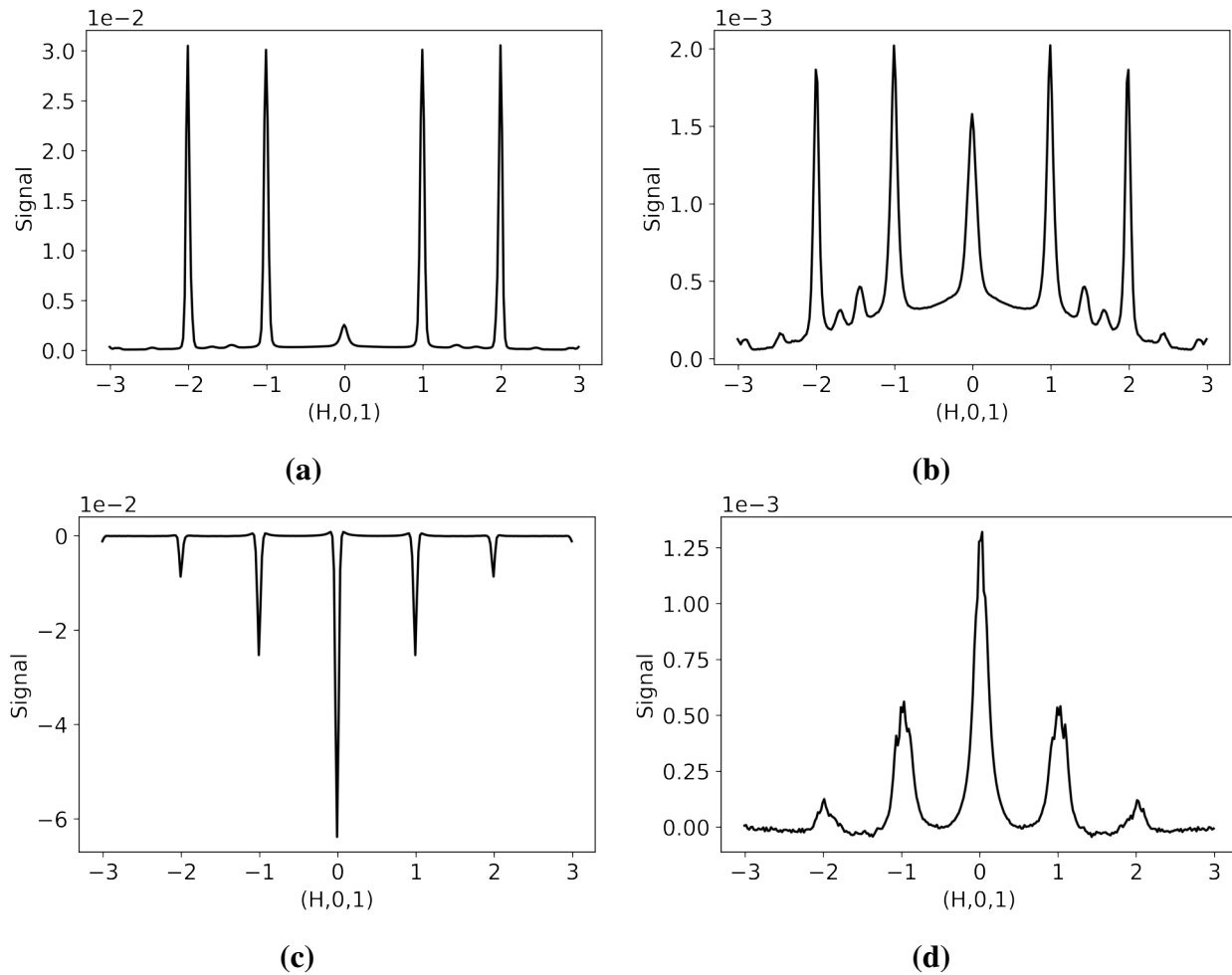


Figure 3.10 (a, b) Cuts taken through the $T \sim 340$ K scattering along the H direction with $K = 0$ and $L = 1$ for before and after Bragg peak removal, respectively. (c, d) Cuts taken through the data where the $T \sim 300$ K scattering was subtracted from the $T \sim 340$ K scattering before and after Bragg peak removal, respectively.

Figure 3.12 shows similar information, but instead where 300 K is subtracted from $T \sim 415$ K. Notice how in general the quality of data deteriorates; both the scattering and the correlations become less defined with each jump in temperature. However, certain trends remain. Both the 370 K and 415 K 3D- Δ mPDF show the warping effect in the inelastic data as discussed earlier in Sec. 3.3. But more importantly, these higher temperature 3D- Δ mPDF exhibit anisotropy in correlation lengths, supportive of the claims that the anisotropic paramagnetic correlations exist up to high temperatures. The strength of these correlations do decrease with increasing temperature, as seen by the lower scaling needed to bring out the features, but this is consistent with the sharp decrease in correlation length as seen in Fig. 3.7(b).

3.4 Conclusion and Future Work

These results give us a unique and intuitive way of analyzing magnetic and atomic structure by providing a real-space view of the atomic correlations in the ordered state of MnTe, and the short-range magnetic correlations in the paramagnetic state of MnTe. Our calculated 3D atomic PDF did not show any definitive signs of short-range atomic features, but still demonstrated that the MnTe atomic lattice could be reconstructed by neutron scattering analysis. Through the 3D- Δ mPDF we were able to visually identify and quantify anisotropy in the magnetic correlations. Then, 1D-mPDF measurements showed that these correlations survive to at least 500 K, and suggest they persist to even higher temperatures due to correlation length stabilization. The consequence is a presence of paramagnons at temperatures where MnTe attains a high zT value, consistent with the proposed theory that paramagnon drag increases thermopower in MnTe. The anisotropic magnetic correlation lengths mean that this enhancement in thermopower is stronger along the c direction than it is within the ab plane. These insights into the nature of the short-range magnetic correlations in MnTe are integral to exploiting the material to its full potential in thermoelectric applications.

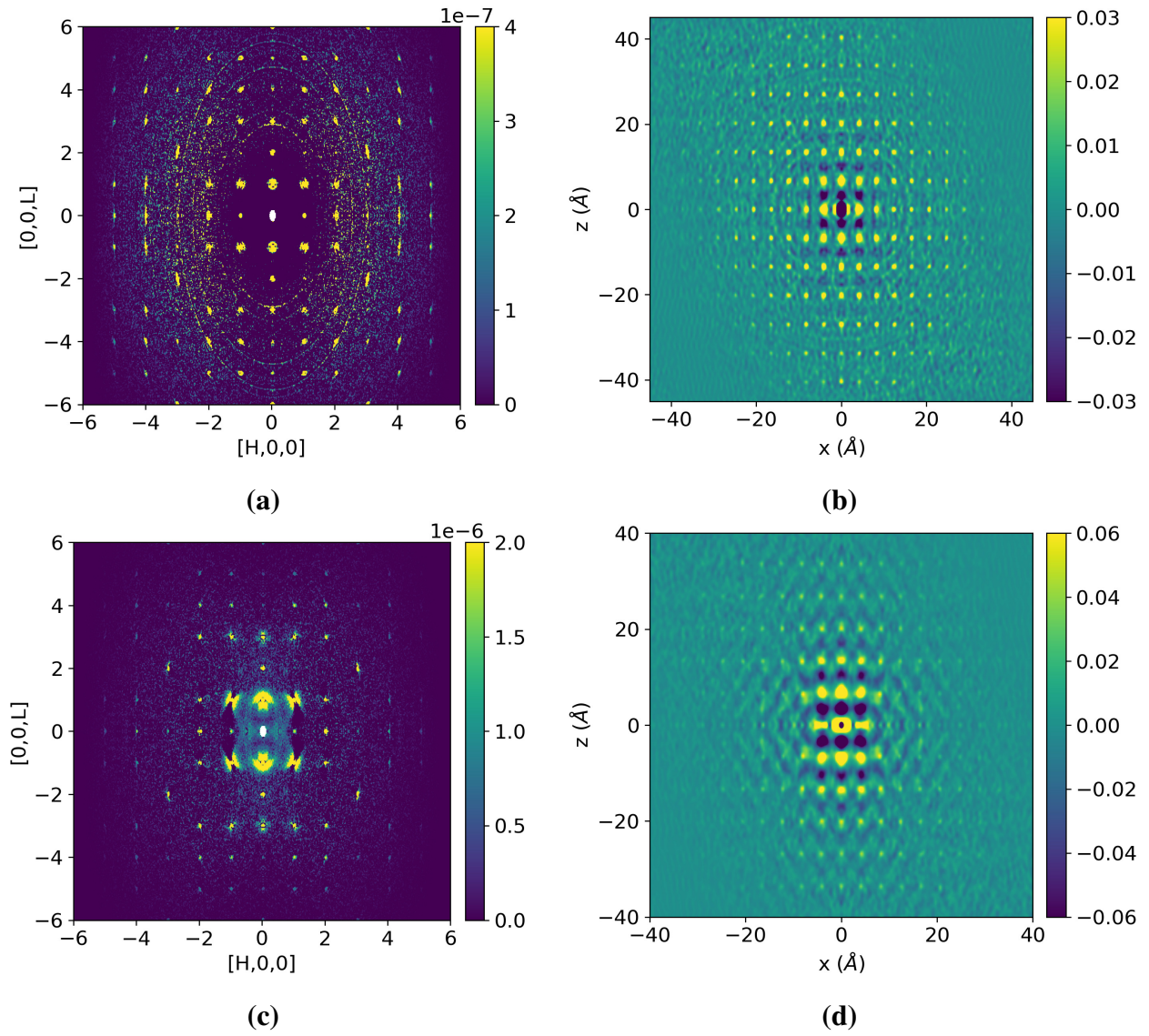


Figure 3.11 (a, c) Intermediate scattering (post subtraction and peak removal) at $T \sim 370$ K in the HOL plane for elastic and inelastic scattering, respectively. (b, d) 3D- $\Delta mPDF$ at $T \sim 370$ K in the $(x, 0, z)$ plane for elastic and inelastic scattering, respectively.

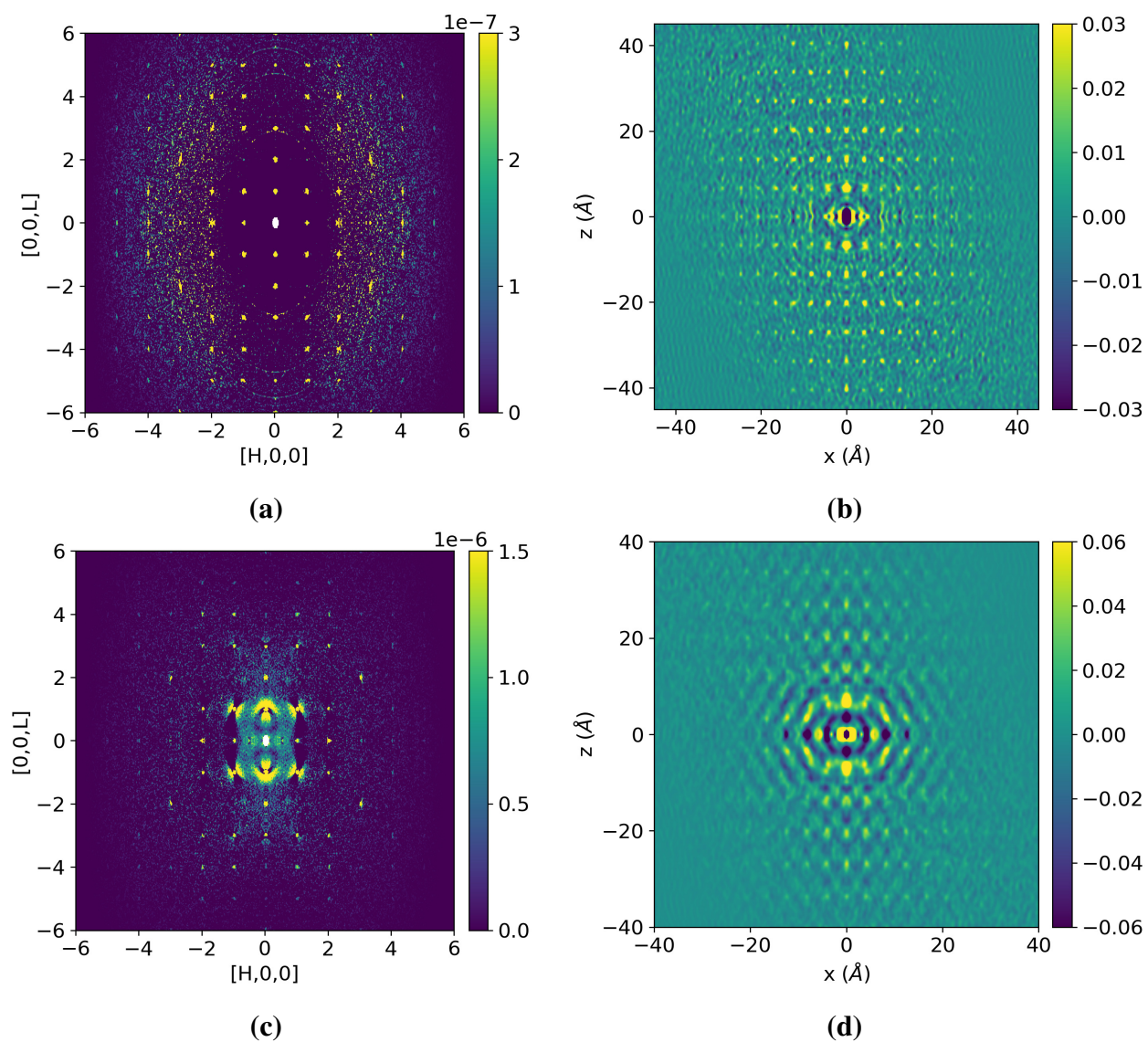


Figure 3.12 (a, c) Intermediate scattering (post subtraction and peak removal) at $T \sim 415$ K in the $H0L$ plane for elastic and inelastic scattering, respectively. (b, d) 3D- Δm PDF at $T \sim 415$ K in the $(x, 0, z)$ plane for elastic and inelastic scattering, respectively.

Computing power and time was a limiting factor in the analysis that could be done during this experiment. The SNS provides a virtual machine (VM) for its users, allowing access to the facility's cluster with plenty of computing power and memory to process our scattering data. However, each 3D-PDF calculation could still take as many as 4 hours to complete, depending on whether or not the input scattering was sliced to be smaller in size. Certain packages and software were not installed on this VM either, such as the `astropy.convolution` package which enables the punch-and-fill method to be used. Because of these limitations, most of the resulting scattering data and PDF had to be transported over to our research group's VM in order to visualize data, save high quality figures, and test the punch-and-fill method. Our VM's lack of memory and computing power relative to the SNS VM made it difficult to properly test the punch-and-fill method. With each file of MnTe single-crystal scattering data being upwards of 6 GB in size, working on multiple files at once was not possible, and time became a factor. If given more time and better computer resources, we could continue to investigate the Mantid punch-and-fill method to possibly find the proper way to use it on our data. Additionally, with more time we could investigate other methods of isolating diffuse scattering besides the ones provided by Mantid. The punch-and-fill method has been implemented in many different ways by other groups, and it is possible that one of these alternative algorithms could provide us with cleaner PDF results.

The powder diffraction data of Fig. 3.2 reveals that doping has an effect on the magnetic structure of MnTe. At this point, not much work has been done to investigate how doping effects the short-range correlations in more detail. This would be important future work, as most semi-conductors are not used in their pure form but only when doped.

The strong foundation laid by our work on MnTe will help us look for similar paramagnon effects in other magnetic semiconductors that could be potential high- zT thermoelectrics. During the time of writing this thesis, our team had the chance to conduct another neutron scattering experiment at the SNS, this time on a single-crystal of TbSb (Terbium Antimony). TbSb is a rare-

earth cubic compound which orders antiferromagnetically below its Neel temperature of $T_N = 15K$. TbSb shows many features which are well-suited for an analysis by the 3D-mPDF method. Like MnTe, the AF interactions found in TbSb are anisotropic in nature [27]. Additionally, intense scattering has been observed while the material is near the Neel temperature transition due to strong short-range correlations just above T_N [28]. The experiment we conducted will allow us to measure the short-range spin correlations in TbSb directly, providing a much more detailed picture of the correlated paramagnetic state above T_N . The information yielded from both the MnTe experiment as well as this experiment will help build a more complete picture of the behaviors of short-range magnetic structures in magnetically enhanced thermoelectrics.

Appendix A

Visualization Package

The purpose of this appendix is to present the code of the Python Visualization package as described in Sec. 2.2.3. Some of the code is not shown as it is unnecessary for understanding functionality. The class contains 4 instance attributes, as shown below.

```
class Visualize:
    """create object containing three-dimensional data
    Args:
        m (numpy array): signal array (3D)
        x (numpy array): x-dimension coordinates (1D)
        y (numpy array): y-dimension coordinates (1D)
        z (numpy array): z-dimension coordinates (1D)
    """
```

The main function in the package is `make_slice`.

```
def make_slice(self, len_a=None, len_b=None, dr=None, use_norm=None,
               cen_pt=None, normal=None, p1=None, p2=None, p3=None):
    """generate a slice through the dataset
```

Args:

*side_len (float): the side length of the square slice
to be taken through the data*

*dr (float): determines the spacing of the grid
(if dr=0.5, then there are 2 measurements every unit)*

*use_norm (boolean): when True, will create slice from a normal vector
and center point. When False, will create slice from three points*

*cen_pt (numpy array): the center of the desired slice.
Used when use_norm is True*

*normal (numpy array): the normal vector to desired plane.
Used when use_norm is True*

*p1, p2, p3 (numpy array): three points in 3D space, each a numpy array.
The plane goes through these points. Used when use_norm is False*

Returns:

*2D array, along with space arrays, representing slice through 3D dataset
"""*

First, the function checks if the user desires to designate a plane by using a center point with normal vector to the plane, or by three points which intersect the plane. If the user desires to use three points, the `three_points` function is accessed.

```
def three_points(self, p1, p2, p3):
    """find normal vector to the plane created by the three given points
    """
```

```
# find two vectors from the three points which lie on the desired plane
vec1 = p2 - p1
vec2 = p3 - p1
# now cross these two vectors to find a vector normal to the plane
normal = np.cross(vec1, vec2)
# now calculate the centroid of the three points given
x_pos = (p1[0] + p2[0] + p3[0]) / 3
y_pos = (p1[1] + p2[1] + p3[1]) / 3
z_pos = (p1[2] + p2[2] + p3[2]) / 3
cen_pt = np.array([x_pos, y_pos, z_pos])
print('Center Point:', cen_pt)

return normal, cen_pt
```

The function returns a center point and normal vector to the `make_slice` function. Now the goal is to create two vectors which lie in the desired plane using the center point and normal vector given by the user.

```
# ensure that our basis vector v1 is not the same as normal
v1 = np.array([1, 0, 0])
if np.allclose(v1, normal):
    v1 = np.array([0, 1, 0])
# now make a matrix which will reflect any vector onto the orthogonal
    # complement of the normal vec, which is our desired plane
# This is done by subtracting from the vector its
    # component along the normal vector
m_norm = np.eye(3) - (np.outer(normal, normal.T) / normal.T.dot(normal))
```

```

# now reflect v1 using m_norm
v1 = m_norm.dot(v1)
# and create a new vector v2 that is orthogonal to both v1 and normal
v2 = np.cross(normal, v1)
# we now have 2 vectors to form our plane

```

These two vectors are used to create a transformation matrix Q which rotates any arbitrary slice to the orientation we want.

```

# now create and normalize Q, which will rotate an arbitrary
  slice to the orientation we desire
Q = np.column_stack((v1, v2, np.zeros_like(v1)))
Q[:, :2] /= np.linalg.norm(Q[:, :2], axis = 0)

```

We now create an arbitrary slice with the side lengths and resolution given by the user.

```

# now create an arbitrary slice
a = np.arange(-len_a / 2, len_a / 2, dr)
b = np.arange(-len_b / 2, len_b / 2, dr)
a = np.append(a, len_a / 2)
b = np.append(b, len_b / 2)
A,B = np.meshgrid(a, b)
# the slice starts on the x-y plane
locations = np.array([A.reshape(-1), B.reshape(-1), np.zeros(A.size)])

```

And we use our transformation matrix Q to rotate the slice, and the center point given by the user to translate the slice into its final position.

```

# now move locations onto our two vectors,

```

```
    # and add cen_pt to move slice into position
locations = Q.dot(locations).T + (cen_pt)
```

Finally, we need to interpolate the 3D data array over this slice

```
    # now we need to interpolate our 3D data array over this slice
points = (self.x, self.y, self.z)
    # find the values of the 3D data array at the slice locations
interp = interpn(points, self.m, locations)
    # obtain the final 2D slice
slice1 = interp.reshape(len(b), len(a))

return slice1, a, b
```

The 2D slice and its 1D spatial arrays are returned to the user to be plotted and analyzed as desired.

Appendix B

Punch-and-fill Method

The purpose of this appendix is to present results using the alternative method of Bragg peak removal, the punch-and-fill method.

Figure B.1 shows the results of using the DeltaPDF3D punch-and-fill method to calculate the 3D- Δ mPDF, for both inelastic and elastic scattering at $T \sim 340$ K. In order to properly identify the locations of the Bragg peaks, the MnTe space group (194) was passed to the function, a designation for the symmetry of the crystal in three-dimensions. Additionally, the user can choose the size of the holes to punch out as well as the width of the Gaussian functions used to fill those holes. The punch-and-fill method as implemented by Mantid had difficulties in giving reasonable and meaningful results. Adjusting the Gaussian width was the most challenging aspect. When the Gaussian width was set to match the size of the punched holes, the resulting 3D- Δ mPDF pattern was noisy and extensive, filling up the entire space. In order to obtain the results shown in Fig. B.1(b,d), the Gaussian width had to be set to a size which inevitably engulfs some of the magnetic diffuse scattering. Because the elastic diffuse scattering confines itself around the Bragg peak locations more than inelastic diffuse scattering, almost all of the diffuse scattering in Fig. B.1a is covered by the Gaussian functions. Additionally, the punch-and-fill algorithm is meant to fill in the holes with smooth, gradual Gaussian functions. Our results show abrupt signal changes where the Bragg peaks

used to be, behavior that may have adverse effects on the PDF.

The punch-and-fill method fails to fully capture the anisotropy we have confirmed to exist from the KAREN method and 1D-mPDF. Although not certain, this could be because the punch-and-fill method covers up some of the diffuse scattering, and fills in holes with values that may not follow the trend of the diffuse scattering near the Bragg peaks. Also, notice how the Gaussians in the intermediate scattering are negative rather than positive like the signal from scattering should appear. This happens because of the over-subtraction causing negative Bragg peaks before the algorithm is ran. Because the punch-and-fill algorithm makes no attempts to find the trend in the data around the Bragg peaks, it simply fills in the negative signal with a negative Gaussian, resulting in a flipped pattern in the 3D- Δ mPDF (Fig. B.1(b,d)), not representative of the MnTe magnetic structure.

The 3D- Δ mPDF from the inelastic scattering is missing the "peanut" effect found in all other inelastic 3D- Δ mPDF analyzed in this thesis. Analysis of the inelastic intermediate scattering of Fig. B.1c shows that the wedges so prominent in the intermediate scattering resulting from KAREN are mostly filled in by the Gaussian functions. This is supportive of the hypothesis that the warping effect is caused by the wedges themselves.

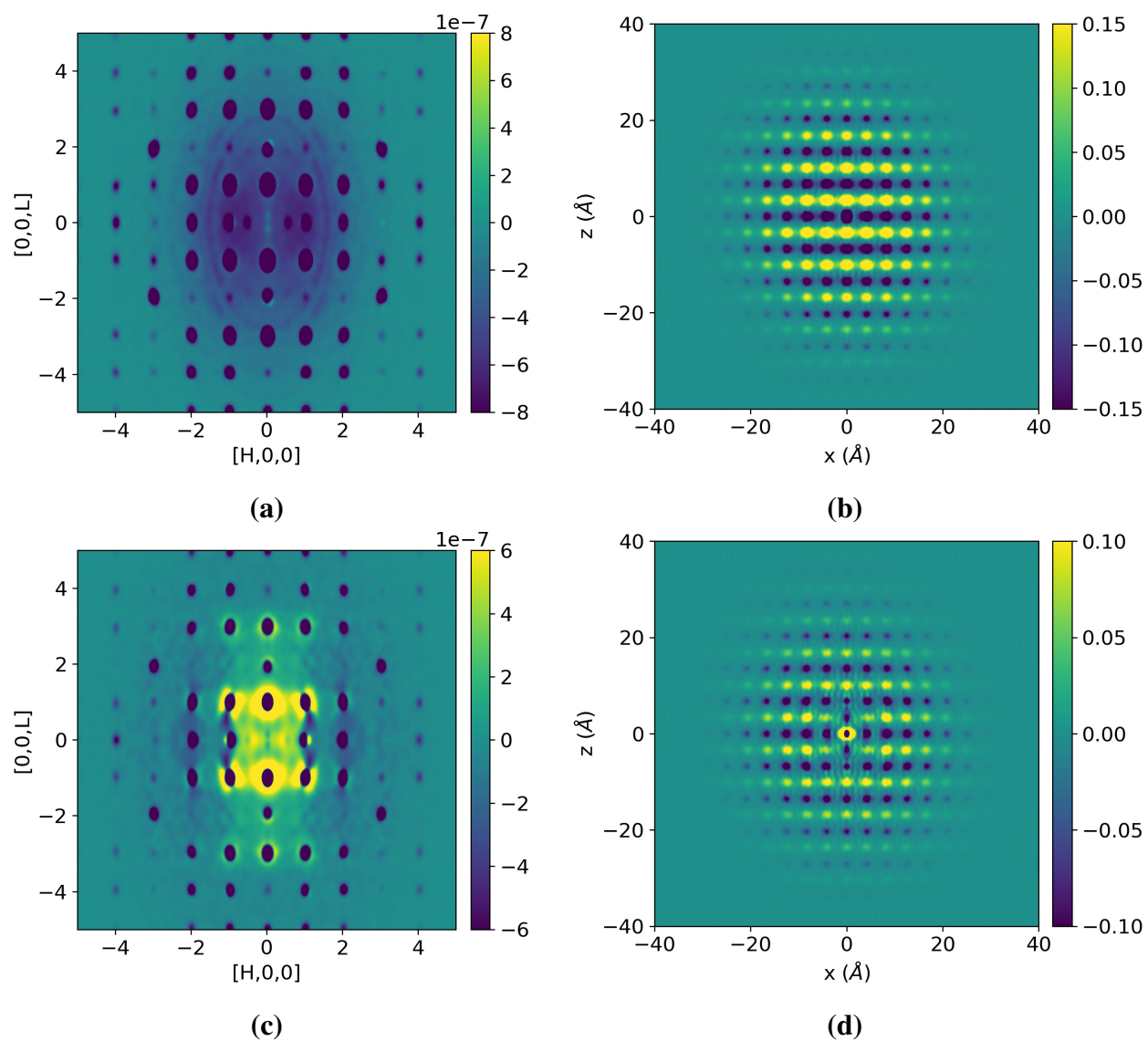


Figure B.1 (a, c) Intermediate scattering (post subtraction and punch-and-fill) at $T \sim 340$ K in the $H0L$ plane for elastic and inelastic scattering, respectively. (b, d) $3D-\Delta mPDF$ at $T \sim 340$ K in the $(x, 0, z)$ plane for elastic and inelastic scattering, respectively.

Bibliography

- [1] Electrical4U, “Seebeck Effect: What is it? (Voltage, Coefficient & Equation),” <https://www.electrical4u.com/seebeck-effect-and-seebeck-coefficient/> (Accessed March 29, 2022).
- [2] J. Mao, G. Chen, and Z. Ren, “Thermoelectric cooling materials,” *Nature Materials* (2020).
- [3] P. A. Finn, C. Asker, K. Wan, E. Bilotti, O. Fenwick, and C. B. Nielsen, “Thermoelectric Materials: Current Status and Future Challenges,” *Frontiers in Electronic Materials* 1 (2021).
- [4] M. Baily, “Maximum Variational Principle for Conduction Problems in a Magnetic Field, and the Theory of Magnon Drag,” *Phys. Rev.* **126**, 2040–2054 (1962).
- [5] F. J. Blatt, D. J. Flood, V. Rowe, P. A. Schroeder, and J. E. Cox, “Magnon-Drage Thermopower in Iron,” *Phys. Rev. Lett.* **18**, 395–396 (1967).
- [6] M. M. H. Polash, F. Mohaddes, M. Rasoulianboroujeni, and D. Vashae, “Magnon-drag thermopower in antiferromagnets versus ferromagnets,” *J. Mater. Chem. C* **8**, 4049–4057 (2020).
- [7] T. Peake, “Paramagnetic Spins Take Electrons for a Ride, Produce Electricity from Heat,” <https://news.ncsu.edu/2019/09/paramagnon-drag-thermopower/> (Accessed March 30, 2022).
- [8] Y. Zheng *et al.*, “Paramagnon drag in high thermoelectric figure of merit Li-doped MnTe,” *Science Advances* **5**, eaat9461 (2019).

- [9] W. H. Bragg and W. L. Bragg, “The reflection of X-rays by crystals,” *Proceedings of the Royal Society of London. Series A, Containing Papers of a Mathematical and Physical Character* **88**, 428–438 (1913).
- [10] T. Egami and S. J. Billinge, “Underneath the Bragg Peaks : Structural Analysis of Complex Materials.,” 2012, iD: 819635623.
- [11] B. Eifert, “Crystal Lattices in Reciprocal Space,” <https://demonstrations.wolfram.com/CrystalLatticesInReciprocalSpace/> (Accessed March 30, 2022).
- [12] N. Ashcroft, A. W. Mermin, N. Mermin, and B. P. Company, *Solid State Physics, HRW international editions* (Holt, Rinehart and Winston, 1976).
- [13] T. Proffen, S. J. L. Billinge, T. Egami, and D. Louca, “Structural analysis of complex materials using the atomic pair distribution function — a practical guide,” *Zeitschrift für Kristallographie - Crystalline Materials* **218**, 132–143 (2003).
- [14] B. A. Frandsen, X. Yang, and S. J. L. Billinge, “Magnetic pair distribution function analysis of local magnetic correlations,” *Acta Crystallographica Section A* **70**, 3–11 (2014).
- [15] B. A. Frandsen and S. J. L. Billinge, “Magnetic structure determination from the magnetic pair distribution function (mPDF): ground state of MnO,” *Acta Crystallographica Section A* **71**, 325–334 (2015).
- [16] N. Roth, A. F. May, F. Ye, B. C. Chakoumakos, and B. B. Iversen, “Model-free reconstruction of magnetic correlations in frustrated magnets,” *IUCrJ* **5**, 410–416 (2018).
- [17] F. Ye, Y. Liu, R. Whitfield, R. Osborn, and S. Rosenkranz, “Implementation of cross correlation for energy discrimination on the time-of-flight spectrometer CORELLI,” *Journal of Applied Crystallography* **51**, 315–322 (2018).

- [18] J. Neuefeind, M. Feygenson, J. Carruth, R. Hoffmann, and K. Chipley, “The Nanoscale Ordered MAterials Diffractometer NOMAD at the Spallation Neutron Source SNS,” *Nuclear Instruments and Methods in Physics Research Section B Beam Interactions with Materials and Atoms* **287**, 68 (2012).
- [19] O. Arnold *et al.*, “Mantid—Data analysis and visualization package for neutron scattering and μ SR experiments,” *Nuclear Instruments and Methods in Physics Research Section A: Accelerators, Spectrometers, Detectors and Associated Equipment* **764**, 156–166 (2014).
- [20] W. R. Busing and H. A. Levy, “Angle calculations for 3- and 4-circle X-ray and neutron diffractometers,” *Acta Crystallographica* **22**, 457–464 (1967).
- [21] J. Weng, E. D. Dill, J. D. Martin, R. Whitfield, C. Hoffmann, and F. Ye, “K-space algorithmic reconstruction (KAREN): a robust statistical methodology to separate Bragg and diffuse scattering,” *Journal of Applied Crystallography* **53**, 159–169 (2020).
- [22] C. L. Farrow, P. Juhas, J. W. Liu, D. Bryndin, E. S. Božin, J. Bloch, T. Proffen, and S. J. L. Billinge, “PDFfit2 and PDFgui: computer programs for studying nanostructure in crystals,” *Journal of Physics: Condensed Matter* **19**, 335219 (2007).
- [23] P. Juhás, C. L. Farrow, X. Yang, K. R. Knox, and S. J. L. Billinge, “Complex modeling: a strategy and software program for combining multiple information sources to solve ill posed structure and nanostructure inverse problems,” *Acta Crystallographica Section A* **71**, 562–568 (2015).
- [24] W. Szuszkiewicz, E. Dynowska, B. Witkowska, and B. Hennion, “Spin-wave measurements on hexagonal MnTe of NiAs-type structure by inelastic neutron scattering,” *Phys. Rev. B* **73**, 104403 (2006).

-
- [25] S. Mu, R. P. Hermann, S. Gorsse, H. Zhao, M. E. Manley, R. S. Fishman, and L. Lindsay, “Phonons, magnons, and lattice thermal transport in antiferromagnetic semiconductor MnTe,” *Phys. Rev. Materials* **3**, 025403 (2019).
- [26] I. Hughes, M. Däne, A. Ernst, H. Wolfram, M. Lueders, J. Staunton, Z. Szotek, and W. Temmerman, “Onset of magnetic order in strongly-correlated systems from ab initio electronic structure calculations: application to transition metal oxides,” *New Journal of Physics* **10** (2008).
- [27] P. J. von Ranke, P. O. Ribeiro, A. M. G. Carvalho, B. P. Alho, T. S. T. Alvarenga, E. P. Nobrega, A. Caldas, V. S. R. de Sousa, P. H. O. Lopes, and N. A. de Oliveira, “Theoretical investigation on the magnetic and electric properties in TbSb compound through an anisotropic microscopic model,” *Journal of Applied Physics* **119**, 183903 (2016).
- [28] R. L. Singh and S. B. Woods, “Critical scattering of electrons near the antiferromagnetic transition of TbSb,” *Phys. Rev. B* **19**, 1555–1560 (1979).

Index

Antiferromagnetic, 5
Bragg Scattering, 9
Correlation Chopper, 22
Correlation Length, 38
Correlations, 14
DeltaPDF3D, 28
DIFFPY, 30
Diffuse Scattering, 9
Elastic Scattering, 8
Ferromagnetic, 5
Fourier Transform, 13
Inelastic Scattering, 9
KAREN, 28
Magnetic Exchange Interaction, 43
Magnon, 5
Manganese Telluride, 7
Mantid Crystallographic Software, 27
Neutron Scattering, 7
Pair Distribution Function, 13
Paramagnon, 5
Powder Diffraction, 21
Punch-and-Fill, 28
Q-space, 10
Single-Crystal Diffraction, 21
Spallation, 22
Spin, 4
Terbium Antimony, 51
Thermoelectric Figure of Merit, 4
Thermoelectric Materials, 3
Total Scattering, 9
Visualization Package, 29